



1 **A Novel Transformation of the Ice Sheet Stokes Equations and**
2 **Some of its Properties and Applications**

3
4 John K. Dukowicz

5 Guest Scientist, Group T-3, Los Alamos National Laboratory,
6 Los Alamos, New Mexico, 87545, USA

7 *Correspondence to:* John K. Dukowicz (jn.dk@outlook.com)
8

9 **Abstract.** A full-Stokes model provides the most accurate but also the most
10 expensive representation of ice sheet dynamics. The Blatter-Pattyn model is a widely
11 used less expensive approximation that is valid for ice sheets characterized by a small
12 aspect ratio. Here we introduce a novel transformation of the Stokes equations into a
13 form that closely resembles the Blatter-Pattyn equations. The transformed exact Stokes
14 equations only differ from the approximate Blatter-Pattyn equations by a few additional
15 terms, while their variational formulations differ only by the presence of a single term in
16 each horizontal direction (one term in 2D and two terms in 3D). Specifically, the
17 variational formulations differ only by the absence (or the neglect) of the vertical velocity
18 in the second invariant of the strain rate tensor in the Blatter-Pattyn model when
19 compared to the Stokes case. Here we make use of the new transformation in two
20 different ways. First, we consider incorporating the transformed equations into a code
21 that can be very easily converted from a Stokes to a Blatter-Pattyn model, and vice-versa,
22 simply by switching these terms on or off. This may be generalized so that the Stokes
23 model is switched on adaptively only where the Blatter-Pattyn model loses accuracy,
24 hopefully retaining most of the accuracy of the Stokes model but at a lower cost. Second,
25 the key role played by the vertical velocity in converting the transformed Stokes model
26 into the Blatter-Pattyn model motivates new approximations that improve on the Blatter-
27 Pattyn model, heretofore the best approximate ice sheet model. These applications
28 require the use of a grid that enables the discrete continuity equation to be invertible for
29 the vertical velocity in terms of the horizontal velocity components. Examples of such
30 grids, such as the first order P1-E0 grid and the second order P2-E1 grid are given in both
31 2D and 3D. It should be noted, however, that the transformed Stokes model has the same
32 type of gravity forcing as the Blatter-Pattyn model, i.e., determined by the slope of the ice
33 sheet upper surface, thereby forgoing some of the grid-generality of the traditional
34 formulation of the Stokes model. This is not a serious disadvantage, however, since in
35 practice it has not impaired the widespread use of the Blatter-Pattyn model.
36



37 **1 Introduction**

38

39 Concern and uncertainty about the magnitude of sea level rise due to melting of the
40 Greenland and Antarctic ice sheets have led to increased interest in improved ice sheet
41 and glacier modeling. The gold standard is a full-Stokes model (i.e., a model that solves
42 the nonlinear, non-Newtonian Stokes system of equations for incompressible ice sheet
43 dynamics) because it is applicable to all geometries and flow regimes. However, the
44 Stokes model is computationally demanding and expensive to solve. It is a nonlinear,
45 three-dimensional model involving four variables, namely, the three velocity components
46 and pressure. In addition, pressure is a Lagrange multiplier enforcing incompressibility
47 and this creates a more difficult indefinite “saddle point” problem. As a result, full-
48 Stokes models exist but are not commonly used in practice (examples are FELIX-S, Leng
49 et al., 2012; Elmer/Ice, Gagliardini et al., 2013).

50

51 Because of these difficulties with the Stokes model, there is much interest in
52 simpler and cheaper approximate models. There is a hierarchy of very simple models
53 such as the shallow ice (SIA) and shallow-shelf (SSA) models, and there are also various
54 higher-order approximations. These culminate in the Blatter-Pattyn (BP) approximation
55 (Blatter, 1995; Pattyn, 2003), which is currently used in production code packages such
56 as ISSM (Larour et al., 2012), MALI (Hoffman et al., 2018; Tezaur et al., 2015) and
57 CISM (Lipscomb et al., 2019). This approximation is based on the assumption of a small
58 ice sheet aspect ratio, i.e., $\varepsilon = H/L \ll 1$, where H, L are the vertical and horizontal
59 length scales, and consequently it eliminates certain stress terms and implicitly assumes
60 small basal slopes. Both the Stokes and Blatter-Pattyn models are described in detail in
61 Dukowicz et al. (2010), hereafter referred to as DPL (2010). Although the Blatter-Pattyn
62 model is reasonably accurate for large-scale motions, accuracy deteriorates for small
63 horizontal scales, less than about five ice thicknesses in the ISMIP–HOM model
64 intercomparison (Pattyn et al., 2008; Perego et al., 2012), or below a 1 km resolution as
65 found in a detailed comparison with full Stokes calculations (Rückamp et al., 2022). This
66 can become particularly important for calculations involving details near the grounding
67 line where the full accuracy of the Stokes model is needed (Nowicki and Wingham,
68 2008). Attempts to address the problem while avoiding the use of full Stokes solvers
69 include variable grid resolution coupled with a Blatter-Pattyn solver (Hoffman et al.,
70 2018) and variable model complexity, where a Stokes solver is embedded locally in a



71 lower order model (Seroussi et al., 2012). Better approximations, more accurate than
72 Blatter-Pattyn but cheaper than Stokes, are not currently available.

73

74 The present paper introduces two innovations that may begin to address some of
75 these issues. The first is a novel transformation of the Stokes model, described in §3,
76 which puts it into a form closely resembling the Blatter-Pattyn model and differing only
77 by the presence of a few extra terms. This allows a code to be switched over from Stokes
78 to Blatter-Pattyn, and vice-versa, globally or locally, by the use of a single parameter that
79 turns off these extra terms. As a result, variable model complexity can be very simply
80 implemented, as described in §6.1. The second innovation is the introduction of new
81 finite element grids that decouple the discrete continuity equation and allow it to be
82 solved for the vertical velocity in terms of the horizontal velocity components. Several
83 elements that may be used to construct such grids are described in Appendix C in both
84 2D and 3D, primarily the first order P1-E0 and second order P2-E1 elements (these two
85 elements are so-named because they employ edge-based pressures). Within the
86 framework of the transformed Stokes model these grids facilitate new approximations
87 that improve on the Blatter-Pattyn approximation so that it is no longer strictly limited to
88 a small ice sheet aspect ratio. We describe two such approximations in §6.2. There is
89 another very significant benefit. A conventional ice sheet Stokes model discretized on
90 such a grid is numerically equivalent to an inherently stable positive-definite
91 minimization (i.e., optimization) problem, as demonstrated in Appendix D. This is in
92 contrast to the ubiquitous Stokes finite element practice of needing to use elements that
93 satisfy the “inf-sup” or “LBB” condition for stability (see Elman et al., 2014, and the
94 brief discussion in §4.3.1).

95

96 **2 The Standard Formulation of the Stokes Ice Sheet Model**

97 **2.1 The Assumed Ice Sheet Configuration**

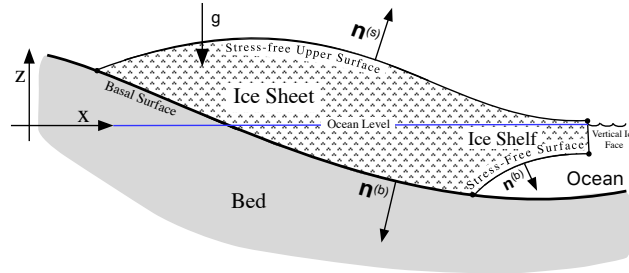
98

99 An ice sheet may be divided into two parts, a part in contact with the bed and a floating
100 ice shelf located beyond the grounding line. The Stokes ice sheet model is capable of
101 describing the flow of an arbitrarily shaped ice sheet, including a floating ice shelf as
102 illustrated in Fig. 1, given appropriate boundary conditions (e.g., Cheng et al., 2020).
103 One limitation of the methods proposed here, in common with the Blatter-Pattyn model,
104 will be that upper and basal surfaces must be able to be connected by a vertical line of sight,



105 as is the case in Fig. 1. Here, for simplicity, we will only consider a fully grounded ice
 106 sheet with periodic lateral boundary conditions, i.e., no ice shelf.

107



108

109

110 **Figure 1** A simplified illustration of the admissible ice sheet configuration.

111

112 Referring to Fig. 1, the entire surface of the ice sheet is denoted by S . An upper

113 surface, labeled S_s and specified by $\zeta_s(x, y, z) = z - z_s(x, y) = 0$, is exposed to the

114 atmosphere and thus experiences stress-free boundary conditions. The bottom or basal

115 surface, denoted by S_B and specified by $\zeta_b(x, y, z) = z - z_b(x, y) = 0$, is in contact with

116 the bed. The basal surface may be subdivided into two sections, $S_B = S_{B1} + S_{B2}$, where

117 S_{B1} , specified by $z = z_{b1}(x, y)$, is the part where ice is frozen to the bed (a no-slip

118 boundary condition), and S_{B2} , specified by $z = z_{b2}(x, y)$, is where frictional sliding

119 occurs. We assume Cartesian coordinates such that $x_i = (x, y, z)$ are position coordinates

120 with $z = 0$ at the ocean surface, and the index $i \in \{x, y, z\}$ represents the three Cartesian

121 indices. Later we shall have occasion to introduce the restricted index $(i) \in \{x, y\}$ to

122 represent just the two horizontal indices. The associated unit normal vectors are $n_i^{(s)}$,

123 $n_i^{(b1)}$, $n_i^{(b2)}$ at the stress-free and basal surfaces, respectively. For the particular geometry

124 illustrated in Fig. 1 we see that $n_z^{(s)} > 0$ and $n_z^{(b1)}, n_z^{(b2)} < 0$. Unit normal vectors

125 appropriate for the ice sheet configuration of Fig. 1 are given by



$$n_i^{(s)} = \left(n_x^{(s)}, n_y^{(s)}, n_z^{(s)} \right) = \frac{\partial \zeta_s(x, y, z) / \partial x_i}{\left| \partial \zeta_s(x, y, z) / \partial x_i \right|} = \frac{(-\partial z_s / \partial x, -\partial z_s / \partial y, 1)}{\sqrt{1 + (\partial z_s / \partial x)^2 + (\partial z_s / \partial y)^2}},$$

$$n_i^{(b)} = \left(n_x^{(b)}, n_y^{(b)}, n_z^{(b)} \right) = -\frac{\partial \zeta_b(x, y, z) / \partial x_i}{\left| \partial \zeta_b(x, y, z) / \partial x_i \right|} = \frac{(\partial z_b / \partial x, \partial z_b / \partial y, -1)}{\sqrt{1 + (\partial z_b / \partial x)^2 + (\partial z_b / \partial y)^2}}.$$

127

128 2.2 The Stokes Equations

129

130 The Stokes model is given by a system of nonlinear partial differential equations and
 131 associated boundary conditions (Greve and Blatter, 2009; DPL, 2010). In a Cartesian
 132 coordinate system the Stokes equations, the three momentum equations and the
 133 continuity equation, for the three velocity components $u_i = (u, v, w)$ and the pressure P
 134 are given by

$$\frac{\partial \tau_{ij}}{\partial x_j} - \frac{\partial P}{\partial x_i} + \rho g_i = 0, \quad (2)$$

$$\frac{\partial u_i}{\partial x_i} = 0, \quad (3)$$

137 where ρ is the density, and g_i is the acceleration due to gravity vector, arbitrarily
 138 oriented in general but here taken to be oriented in the negative z-direction,

139 $g_i = (0, 0, -g)$. Repeated indices imply summation (the Einstein notation). The

140 deviatoric stress tensor τ_{ij} is given by

$$\tau_{ij} = 2\mu_n \dot{\epsilon}_{ij}, \quad (4)$$

142 where μ_n is a nonlinear ice viscosity defined by

$$\mu_n = \eta_0 \left(\dot{\epsilon}^2 \right)^{(1-n)/2n}, \quad (5)$$

144 and $\dot{\epsilon}^2 = \dot{\epsilon}_{ij} \dot{\epsilon}_{ij} / 2$ is the second invariant of the strain rate tensor $\dot{\epsilon}_{ij}$. The strain rate
 145 tensor is given by

$$\dot{\epsilon}_{ij} = \frac{1}{2} \left(\frac{\partial u_i}{\partial x_j} + \frac{\partial u_j}{\partial x_i} \right), \quad (6)$$

147 and therefore the second invariant may be written out as



$$148 \quad \dot{\epsilon}^2 = \frac{1}{2} \left[\left(\frac{\partial u}{\partial x} \right)^2 + \left(\frac{\partial v}{\partial y} \right)^2 + \left(\frac{\partial w}{\partial z} \right)^2 \right] + \frac{1}{4} \left[\left(\frac{\partial u}{\partial y} + \frac{\partial v}{\partial x} \right)^2 + \left(\frac{\partial u}{\partial z} + \frac{\partial w}{\partial x} \right)^2 + \left(\frac{\partial v}{\partial z} + \frac{\partial w}{\partial y} \right)^2 \right]. \quad (7)$$

149 Note that the second invariant is positive-definite, i.e., $\dot{\epsilon}^2 \geq 0$. As usual, ice is assumed
 150 to obey Glen's flow law, where n is the Glen's law exponent ($n = 1$ for a linear
 151 Newtonian fluid, and typically $n = 3$ in ice sheet modeling, resulting in a nonlinear non-
 152 Newtonian fluid). The coefficient η_0 is defined by $\eta_0 = A^{-1/n} / 2$, where A is an ice flow
 153 factor, here taken to be a constant but in general depending on temperature and other
 154 variables (see Schoof and Hewitt, 2013). The three-dimensional Stokes system (2), (3)
 155 requires a set of boundary conditions at every bounding surface, each set being composed
 156 of three components. Aside from the periodic lateral boundary conditions used in our test
 157 problems, the relevant boundary conditions are as follows

158 (1) Stress-free boundary conditions on surfaces S_s not in contact with the bed, such
 159 as the upper surface S_s :

$$160 \quad \tau_{ij} n_j^{(s)} - P n_i^{(s)} = 0. \quad (8)$$

161 The basal boundary conditions are given by

162 (2) No-slip or frozen to the bed conditions on surface segment S_{B1} :

$$163 \quad u_i = 0 \quad (9)$$

164 (3) Frictional tangential sliding conditions on surface segment S_{B2} :

165 Frictional conditions are more complicated and are discussed in detail in Appendix A. In
 166 summary, these conditions are composed of two parts,

167 (3a) A single condition enforcing tangential flow at the basal surface:

$$168 \quad u_i n_i^{(b2)} = 0. \quad (10)$$

169 (3b) Two conditions specifying the horizontal components of the tangential
 170 frictional stress force vector. From Appendix A, the simplest representation of these two
 171 conditions is

$$172 \quad n_z^{(b2)} \left(\tau_{(i)j} n_j^{(b2)} + f_{(i)} \right) - n_{(i)}^{(b2)} \left(\tau_{zj} n_j^{(b2)} + f_z \right) = 0, \quad (11)$$

173 where $(i) \in \{x, y\}$ is the notation previously introduced for restricted (horizontal) indices,

174 and f_i is a specified frictional sliding force vector, tangential to the bed ($n_i^{(b2)} f_i = 0$).



175 This is potentially a complicated function of position and velocity (e.g., Schoof, 2010),
 176 however, here we assume only simple linear frictional sliding,

$$177 \quad f_i = \beta(x) u_i, \quad (12)$$

178 where $\beta(x) > 0$ is a position-dependent drag law coefficient. For simplicity we assume
 179 there is no melting or refreezing at the bed resulting in vertical inflows or outflows. If
 180 needed, these can be easily added (Dukowicz et al., 2010; Heinlein et al., 2022).

181

182 **2.3 The Stokes Variational Principle**

183

184 A variational principle, if available, is usually the most compact way of representing a
 185 particular problem. The Stokes model possesses a variational principle that is
 186 particularly useful for discretization purposes and for the specification of boundary
 187 conditions (see DPL, 2010, for a fuller description of the variational principle applied to
 188 ice sheet modeling). There are a number of significant advantages. For example, all
 189 boundary conditions are conveniently incorporated in the variational formulation, all
 190 terms in the variational functional, including boundary condition terms, contain lower
 191 order derivatives than in the momentum equations, and the solution of the discrete
 192 problem automatically involves a symmetric matrix. In discretizing the momentum
 193 equations, stress terms at boundaries involve derivatives that require information from
 194 across boundaries. This problem does not arise in the variational formulation since all
 195 terms are evaluated in the interior. Finally, stress-free boundary conditions, as at the
 196 upper surface for example, need not be specified at all since they are automatically
 197 incorporated in the functional as natural boundary conditions. In discrete applications,
 198 the variational method presented here is closely related to the Galerkin finite element
 199 method, a subset of the weak formulation method in which the test and trial functions are
 200 the same (see Schoof, 2010, in connection with the Blatter-Pattyn model).

201

202 The variational functional for the standard Stokes model may be written in two
 203 alternative forms:

204 (1) Basal boundary conditions imposed using Lagrange multipliers:

$$205 \quad \mathcal{A}[u_i, P, \lambda_i, \Lambda] = \int_V dV \left[\frac{4n}{n+1} \eta_0 (\dot{\epsilon}^2)^{(1+n)/2n} - P \frac{\partial u_i}{\partial x_i} + \rho g w \right] \\ + \int_{S_{B1}} dS \lambda_i u_i + \int_{S_{B2}} dS \left[\Lambda u_i n_i^{(b2)} + \frac{1}{2} \beta(x) u_i u_i \right], \quad (13)$$



206 where λ_i and Λ are Lagrange multipliers used to enforce the no-slip condition and
207 frictional tangential sliding, respectively. As in DPL (2010), arguments enclosed in
208 square brackets, here $u_i, P, \lambda_i, \Lambda$, indicate those variables that are used in the variation of
209 the functional.

210 (2) Basal boundary conditions imposed by direct substitution:

211 In this case, the two conditions (9), (10) are used directly in the functional to specify all
212 three velocity components u_i in the first case, and the vertical velocity w in terms of the
213 horizontal velocity components in the second case, along the entire basal boundary in
214 both the volume and surface integrals in (13). In particular, (10) is used in the following
215 form,

$$216 \quad w = -\frac{u_{(i)} n_{(i)}^{(b2)}}{n_z^{(b2)}} = u_{(i)} \frac{\partial z_b}{\partial x_{(i)}}, \quad (14)$$

217 to replace w in terms of the horizontal velocity components $u_{(i)}$ on the basal boundary
218 segment S_{B2} . Here we use z_b as a shorthand notation for $z_b(x, y)$. The variational
219 functional in this case becomes

$$220 \quad \mathcal{A}[u_i, P] = \int_V dV \left[\frac{4n}{n+1} \eta_0 (\dot{\epsilon}^2)^{(1+n)/2n} - P \frac{\partial u_i}{\partial x_i} + \rho g w \right] \\ + \frac{1}{2} \int_{S_{B2}} dS \beta(x) \left(u_{(i)} u_{(i)} + \left(u_{(i)} n_{(i)}^{(b2)} / n_z^{(b2)} \right)^2 \right). \quad (15)$$

221 Note that (14) has been explicitly used to replace w in the basal boundary component of
222 the functional (15) but, importantly, it must also be used in the volume integral part of
223 (15) to replace all values of w that lie on the basal boundary segment S_{B2} .

224

225 As described in DPL (2010), a variational procedure, i.e., taking the variation
226 with respect to the independent functions $u_i, P, \lambda_i, \Lambda$ in (13), and u_i, P in (15), yields the
227 full set of Euler-Lagrange equations and boundary conditions that specify the standard
228 Stokes model, equivalent to (2)-(11). In the case of (13), the system determines all the
229 discrete variables specified on the mesh: the velocity components and the pressure, u_i, P ,
230 together with the Lagrange multipliers, λ_i, Λ . In the case of (15), the system only
231 determines the unspecified velocity variables u_i and the pressure P . The specified



232 values of velocity are then obtainable a posteriori from (9) or (14). As a result, system
233 (15) is smaller and simpler and is therefore the one predominantly used in this paper.

234

235 **3. A Transformation of the Stokes Model**

236 **3.1 Origin of the Transformation**

237

238 The transformation is motivated by the Blatter-Pattyn approximation. Consider the
239 vertical component of the momentum equation and the corresponding stress-free upper
240 surface boundary condition in the Blatter-Pattyn approximation (from DPL, 2010, for
241 example), which are given by

$$\begin{aligned} 242 \quad & \frac{\partial}{\partial z} \left(2\mu_n \frac{\partial w}{\partial z} \right) - \frac{\partial P}{\partial z} - \rho g = 0, \\ & \left(2\mu_n \frac{\partial w}{\partial z} - P \right) n_z^{(s)} = 0 \quad \text{at } z = z_s(x, y). \end{aligned} \quad (16)$$

243 These equations may be rewritten in the form

$$\begin{aligned} 244 \quad & \frac{\partial}{\partial z} \left(P - 2\mu_n \frac{\partial w}{\partial z} + \rho g (z - z_s(x, y)) \right) = 0, \\ & \left(P - 2\mu_n \frac{\partial w}{\partial z} + \rho g (z - z_s(x, y)) \right) n_z^{(s)} = 0 \quad \text{at } z = z_s(x, y). \end{aligned} \quad (17)$$

245 This suggests the introduction of a new variable \tilde{P} , to be called the transformed pressure,

$$246 \quad \tilde{P} = P - 2\mu_n \frac{\partial w}{\partial z} + \rho g (z - z_s(x, y)), \quad (18)$$

247 which simplifies system (17) as follows

$$\begin{aligned} 248 \quad & \frac{\partial \tilde{P}}{\partial z} = 0, \\ & \tilde{P} n_z^{(s)} = 0 \quad \text{at } z = z_s(x, y). \end{aligned} \quad (19)$$

249 This is a complete one-dimensional partial differential system, that, when integrated from
250 the top surface down yields

$$251 \quad \tilde{P} = 0. \quad (20)$$

252 Thus, the transformed pressure vanishes in the Blatter-Pattyn case. The definition (18)

253 forms the basis of the present transformation but we also use the continuity equation to

254 eliminate $\partial w / \partial z$ as is done in the Blatter-Pattyn approximation (see DPL, 2010).



255 Therefore, the transformation consists of eliminating P and $\partial w/\partial z$ in the Stokes system
 256 (2), (4)-(11) (i.e., everywhere except in the continuity equation (3) itself) by means of

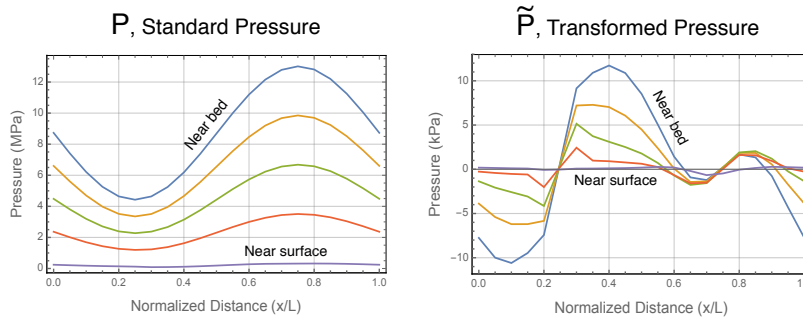
257
$$P = \tilde{P} - 2\mu_n \left(\frac{\partial u}{\partial x} + \frac{\partial v}{\partial y} \right) + \rho g(z_s - z), \quad (21)$$

258
$$\frac{\partial w}{\partial z} = - \left(\frac{\partial u}{\partial x} + \frac{\partial v}{\partial y} \right), \quad (22)$$

259 where z_s is a shorthand notation for $z_s(x, y)$.

260

261 In the standard Stokes system the pressure P is primarily a Lagrange multiplier
 262 enforcing incompressibility but with a very large hydrostatic component. The
 263 transformation eliminates the hydrostatic pressure from \tilde{P} , as illustrated in Fig. 2 where
 264 the two pressures, plotted along grid lines, from Exp. B in the ISMIP–HOM model
 265 intercomparison (Pattyn et al., 2008) at $L = 10$ km are compared. The standard Stokes
 266 pressure P is some three orders of magnitude larger than the transformed pressure \tilde{P} .



267

268 **Figure 2.** Standard pressure P compared to the transformed pressure \tilde{P} in Exp. B from
 269 the ISMIP–HOM model intercomparison. Note that P is in MPa while \tilde{P} is in kPa.

270

271 The transformed pressure \tilde{P} is again a Lagrange multiplier enforcing
 272 incompressibility, i.e., it may be viewed as the effective pressure in the transformed
 273 system. Alternatively, since $\tilde{P} = 0$ in the Blatter-Pattyn approximation, the definition of
 274 \tilde{P} from (18) may be written as $\tilde{P} = P - P_{BP}$, where

275
$$P_{BP} = -2\mu_n \left(\frac{\partial u}{\partial x} + \frac{\partial v}{\partial y} \right) + \rho g(z_s - z)$$



276 is the effective Blatter-Pattyn pressure (Tezaur et al., 2015). As a result, we have
 277 $P = P_{BP} + \tilde{P}$, and therefore \tilde{P} is actually the “Stokes” correction to the Blatter-Pattyn
 278 pressure.

279

280 3.2 The Transformed Stokes Equations

281

282 Introducing (21), (22) into the Stokes system of equations (2)-(11) results in the
 283 following transformed Stokes system:

$$284 \quad \frac{\partial \tilde{\tau}_{ij}}{\partial x_j} - \hat{\xi} \frac{\partial \tilde{P}}{\partial x_i} - \rho g \frac{\partial z_s}{\partial x_{(i)}} = 0, \quad (23)$$

$$285 \quad \hat{\xi} \frac{\partial u_i}{\partial x_i} = 0, \quad (24)$$

286 where quantities that are modified in the transformation are indicated by a tilde, e.g., \tilde{P} .

287 Corresponding to (4), the modified Stokes deviatoric stress tensor $\tilde{\tau}_{ij}$ is given by

$$288 \quad \tilde{\tau}_{ij} = 2\tilde{\mu}_n \left(\tilde{\epsilon}_{ij} + \frac{\partial u_{(i)}}{\partial x_{(i)}} \delta_{ij} \right), \quad (25)$$

289 where δ_{ij} is the Kronecker delta, the modified strain rate tensor $\tilde{\epsilon}_{ij}$, corresponding to (6),

290 is given by

$$291 \quad \tilde{\epsilon}_{ij} = \begin{bmatrix} \frac{\partial u}{\partial x} & \frac{1}{2} \left(\frac{\partial u}{\partial y} + \frac{\partial v}{\partial x} \right) & \frac{1}{2} \left(\frac{\partial u}{\partial z} + \xi \frac{\partial w}{\partial x} \right) \\ \frac{1}{2} \left(\frac{\partial u}{\partial y} + \frac{\partial v}{\partial x} \right) & \frac{\partial v}{\partial y} & \frac{1}{2} \left(\frac{\partial v}{\partial z} + \xi \frac{\partial w}{\partial y} \right) \\ \frac{1}{2} \left(\frac{\partial u}{\partial z} + \xi \frac{\partial w}{\partial x} \right) & \frac{1}{2} \left(\frac{\partial v}{\partial z} + \xi \frac{\partial w}{\partial y} \right) & - \left(\frac{\partial u}{\partial x} + \frac{\partial v}{\partial y} \right) \end{bmatrix} \quad (26)$$

292 and, corresponding to (5), the modified viscosity,

$$293 \quad \tilde{\mu}_n = \eta_0 \left(\tilde{\epsilon}^2 \right)^{(1-n)/2n}, \quad (27)$$

294 is given in terms of the second invariant $\tilde{\epsilon}^2 = \tilde{\epsilon}_{ij} \tilde{\epsilon}_{ij} / 2$, which, in expanded form becomes

$$295 \quad \tilde{\epsilon}^2 = \left(\frac{\partial u}{\partial x} \right)^2 + \frac{\partial u}{\partial x} \frac{\partial v}{\partial y} + \left(\frac{\partial v}{\partial y} \right)^2 + \frac{1}{4} \left[\left(\frac{\partial u}{\partial y} + \frac{\partial v}{\partial x} \right)^2 + \left(\frac{\partial u}{\partial z} + \xi \frac{\partial w}{\partial x} \right)^2 + \left(\frac{\partial v}{\partial z} + \xi \frac{\partial w}{\partial y} \right)^2 \right]. \quad (28)$$



296 The dummy variables $\xi = 1, \hat{\xi} = 1$ identify terms that are dropped in the Blatter-Pattyn
 297 approximation, as explained below. Since (28) differs from (7) only by the use of
 298 substitution (22), the transformation leaves the second invariant $\tilde{\epsilon}^2$ and viscosity $\tilde{\mu}_n$
 299 unchanged provided the continuity equation (24) is satisfied, i.e., $\tilde{\epsilon}^2 = \epsilon^2$ and $\tilde{\mu}_n = \mu_n$,
 300 and in particular, the transformed second invariant remains positive-definite, i.e., $\tilde{\epsilon}^2 \geq 0$.
 301

302 The boundary conditions for the transformed equations, corresponding to (8)-(11),
 303 are given by

304 BCs on S_S :
$$\tilde{\tau}_{ij} n_j^{(s)} - \tilde{\xi} \tilde{P} n_i^{(s)} = 0 , \tag{29}$$

305 BCs on S_{B1} :
$$u_i = 0 , \tag{30}$$

306 BCs on S_{B2} :
$$u_i n_i^{(b2)} = 0 , \tag{31}$$

307
$$n_z^{(b2)} \left(\tilde{\tau}_{(i)j} n_j^{(b2)} + \beta(x) u_{(i)} \right) - n_{(i)}^{(b2)} \left(\tilde{\tau}_{zj} n_j^{(b2)} + \beta(x) u_{(j)} n_{(j)}^{(b2)} / n_z^{(b2)} \right) = 0 . \tag{32}$$

308 Equations (31), (32) constitute the three required boundary conditions for frictional
 309 sliding (see Appendix A). Note that (32) differs from (11) because (14) has been used to
 310 eliminate the vertical velocity component w in favor of the horizontal velocity
 311 components $u_{(i)}$.

312

313 The dummy variables $\xi, \hat{\xi}$ in (23)-(25) and (26)-(29) have been introduced to
 314 identify the terms that are neglected in the two types of the Blatter-Pattyn approximation
 315 that we consider in §3.4. Specifically, these two types are (a) the standard Blatter-Pattyn
 316 approximation, $\xi = 0, \hat{\xi} = 0$, as originally derived (Blatter, 1995; Pattyn, 2003; DPL,
 317 2010), which solves for just the horizontal velocity components u, v , and (b) the extended
 318 Blatter-Pattyn approximation, $\xi = 0, \hat{\xi} = 1$, described more fully later, which contains the
 319 standard approximation and also provides the additional equations for determination of
 320 the consistent vertical velocity component w and pressure \tilde{P} . Keeping all terms, i.e.,
 321 $\xi = 1, \hat{\xi} = 1$, specifies the full transformed Stokes model.

322

323 The transformed system (25)-(32) and the standard Stokes system (2)-(11) yield
 324 exactly the same solution. However, in common with the Blatter-Pattyn approximation,



325 transformation (21) implies the use of a gravity-oriented coordinate system because of the
 326 particular form of the gravitational forcing term, while the standard Stokes model does
 327 not have this restriction. This is only a minor limitation. A somewhat more restrictive
 328 limitation is the appearance of $z_s(x, y)$, an implicitly single valued function, to describe
 329 the vertical position of the upper surface of the ice sheet. This means that care must be
 330 taken in case of reentrant upper surfaces (i.e., S-shaped in 2D) and sloping cliffs at the ice
 331 edge, a restriction not present in the standard Stokes model. As noted earlier, we assume
 332 that the upper and basal surfaces are connected by a vertical line of sight. With a
 333 reentrant ice surface, such a vertical line must be broken up into individual segments with
 334 each segment having its own “upper” surface location $z_s(x, y)$. Fortunately, such
 335 situations do not normally arise in practice. Exactly these same limitations exist in the
 336 Blatter-Patten model, which does not hinder its use in practice.

337

338 3.3 The Transformed Stokes Variational Principle

339

340 It is easy to verify that the transformed Stokes system (23)-(32) results from the variation
 341 with respect to u_i, \tilde{P} of the following functional:

$$\begin{aligned}
 342 \quad \tilde{\mathcal{A}}[u_i, \tilde{P}] = & \int_V dV \left[\frac{4n}{n+1} \eta_0 (\tilde{\epsilon}^2)^{(1+n)/2n} - \hat{\xi} \tilde{P} \frac{\partial u_i}{\partial x_i} + \rho g u_{(i)} \frac{\partial z_s}{\partial x_{(i)}} \right] \\
 & + \frac{1}{2} \int_{S_{B_2}} dS \beta(x) \left(u_{(i)} u_{(i)} + \left(u_{(i)} n_{(i)}^{(b_2)} / n_z^{(b_2)} \right)^2 \right), \quad (33)
 \end{aligned}$$

343 where $\tilde{\epsilon}^2$ is the transformed second invariant from (28). Basal boundary conditions in
 344 (33) are imposed by direct substitution, as in (15). Alternatively, one could impose
 345 boundary conditions using Lagrange multipliers, as in (13), but direct substitution is
 346 preferred because it is simpler and involves fewer variables. The remarks made in §2.3
 347 about replacing all values of w that lie on the basal boundary segment S_{B_2} by (14) apply
 348 here also.

349

350 3.4 Two Blatter-Pattyn Approximations

351 3.4.1 The Standard Blatter-Pattyn Approximation

352

353 The standard (or traditional) Blatter-Pattyn approximation (originally introduced by
 354 Blatter, 1995; Pattyn, 2003; later by DPL, 2010; Schoof and Hewitt, 2013) is obtained by



355 setting $\xi = 0, \hat{\xi} = 0$. This yields the following Blatter-Pattyn variational functional in
 356 terms of horizontal velocity components only,

$$357 \quad \mathcal{A}_{BP}[u_{(i)}] = \int_V dV \left[\frac{4n}{n+1} \eta_0 (\hat{\epsilon}_{BP}^2)^{(1+n)/2n} + \rho g u_{(i)} \frac{\partial z_s}{\partial x_{(i)}} \right] \quad (34)$$

$$+ \frac{1}{2} \int_{S_{B2}} dS \beta(x) \left(u_{(i)} u_{(i)} + \zeta \left(u_{(i)} n_{(i)}^{(b2)} / n_z^{(b2)} \right)^2 \right),$$

358 where

$$359 \quad \hat{\epsilon}_{BP}^2 = \left(\frac{\partial u}{\partial x} \right)^2 + \frac{\partial u}{\partial x} \frac{\partial v}{\partial y} + \left(\frac{\partial v}{\partial y} \right)^2 + \frac{1}{4} \left[\left(\frac{\partial u}{\partial y} + \frac{\partial v}{\partial x} \right)^2 + \frac{\partial u^2}{\partial z} + \frac{\partial v^2}{\partial z} \right], \quad (35)$$

360 and the corresponding Euler-Lagrange equations and boundary conditions are given by

$$361 \quad \frac{\partial \tau_{(ij)}^{BP}}{\partial x_j} - \rho g \frac{\partial z_s}{\partial x_{(i)}} = 0; \quad \begin{cases} \tau_{(ij)}^{BP} n_j^{(b2)} + \beta(x) \left(u_{(i)} + \zeta \left(u_{(i)} n_{(i)}^{(b2)} / n_z^{(b2)} \right) n_{(i)}^{(b2)} / n_z^{(b2)} \right) = 0 \\ \text{on } S_{B2}, \quad \tau_{(ij)}^{BP} n_j^{(s)} = 0 \text{ on } S_S, \quad u_{(i)} = 0 \text{ on } S_{B1}, \end{cases} \quad (36)$$

362 where the Blatter-Pattyn stress tensor $\tau_{(ij)}^{BP}$ is

$$363 \quad \tau_{(ij)}^{BP} = \eta_0 (\hat{\epsilon}_{BP}^2)^{(1-n)/2n} \begin{bmatrix} 2 \left(2 \frac{\partial u}{\partial x} + \frac{\partial v}{\partial y} \right) & \left(\frac{\partial u}{\partial y} + \frac{\partial v}{\partial x} \right) & \frac{\partial u}{\partial z} \\ \left(\frac{\partial u}{\partial y} + \frac{\partial v}{\partial x} \right) & 2 \left(\frac{\partial u}{\partial x} + 2 \frac{\partial v}{\partial y} \right) & \frac{\partial v}{\partial z} \end{bmatrix}. \quad (37)$$

364 There is a new dummy variable ζ in (34) introduced to identify the basal boundary term
 365 that is normally dropped ($\zeta = 0$) in the standard Blatter-Pattyn approximation but which
 366 was restored ($\zeta = 1$) in Dukowicz et al. (2011) to better deal with arbitrary basal
 367 topography.

368

369 The Blatter-Pattyn model is a well-behaved nonlinear approximate system for the
 370 horizontal velocity components u, v because in this case the variational formulation is
 371 actually a convex optimization problem whose solution minimizes the functional. As
 372 noted in the Introduction, the Blatter-Pattyn approximation is widely used in practice as
 373 an economical and relatively accurate ice sheet model. If desired, the vertical velocity
 374 component w is computed a posteriori by means of the continuity equation.

375



376 **Remark #1:** The original formulation (e.g., Pattyn, 2003) also approximates the normal
 377 unit vectors $n_i^{(b2)}$ on the frictional part of the basal boundary S_{B2} by making the small
 378 slope approximation (Dukowicz et al., 2011; Perego et al., 2012). However, this
 379 additional approximation is unnecessary since any computational savings are negligible.

381 3.4.2 The Extended Blatter-Pattyn Approximation

382
 383 A second form of the Blatter-Pattyn approximation is obtained from the transformed
 384 variational principle (33) by making the assumption,

$$385 \quad \left\| \frac{\partial w}{\partial x} \right\| \ll \left\| \frac{\partial u}{\partial z} \right\|, \quad \left\| \frac{\partial w}{\partial y} \right\| \ll \left\| \frac{\partial v}{\partial z} \right\|, \quad (38)$$

386 and therefore neglecting $\partial w/\partial x, \partial w/\partial y$ in the transformed second invariant $\tilde{\epsilon}^2$, or
 387 equivalently, in the strain rate tensor $\tilde{\epsilon}_{ij}$ from (26), consistent with the original small
 388 aspect ratio approximation (Blatter, 1995; Pattyn, 2003; DPL, 2010; Schoof and
 389 Hindmarsh, 2008). This corresponds to setting $\xi = 0, \hat{\xi} = 1$ in the transformed Stokes
 390 model. That is, we neglect vertical velocity gradients but keep the pressure Lagrange
 391 multiplier term. This will be called the extended Blatter-Pattyn approximation (EBP)
 392 because, in contrast to the standard Blatter-Pattyn approximation, all the variables, i.e.,
 393 u, v, w, \tilde{P} , are retained. Notably, assumption (38) is equivalent to just setting $w = 0$ in
 394 the second invariant $\tilde{\epsilon}^2$ in the full transformed Stokes model (i.e., with $\xi = 1, \hat{\xi} = 1$). In
 395 other words, the extended BP approximation is obtained by neglecting vertical velocities
 396 everywhere in (33) except where they occurs in the velocity divergence term. This aspect
 397 of the transformed Stokes model will be exploited later to obtain approximations that
 398 improve on Blatter-Pattyn. Thus, the extended Blatter-Pattyn functional is given by

$$399 \quad \mathcal{A}_{EBP}[u_i, \tilde{P}] = \int_V dV \left[\frac{4n}{n+1} \eta_0 \left(\dot{\epsilon}_{BP}^2 \right)^{(1+n)/2n} - \tilde{P} \frac{\partial u_i}{\partial x_i} + \rho g u_{(i)} \frac{\partial z_s}{\partial x_{(i)}} \right] \\
 + \frac{1}{2} \int_{S_{B2}} dS \beta(x) \left(u_{(i)} u_{(i)} + \varsigma \left(u_{(i)} n_{(i)}^{(b2)} / n_z^{(b2)} \right)^2 \right), \quad (39)$$

400 where the Blatter-Pattyn second invariant $\dot{\epsilon}_{BP}^2$ is given by (35). Taking the variation of
 401 the functional, the resulting system of extended Blatter-Pattyn Euler-Lagrange equations
 402 and their boundary conditions is given by



403 (1) Variation with respect to $u_{(i)}$ yields the horizontal momentum equation:

$$404 \quad \frac{\partial \tau_{(i)j}^{BP}}{\partial x_j} - \frac{\partial \tilde{P}}{\partial x_{(i)}} - \rho g \frac{\partial z_s}{\partial x_{(i)}} = 0; \quad \left\{ \begin{array}{l} \tau_{(i)j}^{BP} n_j^{(s)} - \tilde{P} n_{(i)}^{(s)} = 0 \text{ on } S_S, \quad u_{(i)} = 0 \text{ on } S_{B1}, \\ \tau_{(i)j}^{BP} n_j^{(b2)} + \beta(x) \left(u_{(i)} + \zeta \left(u_{(k)} n_{(k)}^{(b2)} / n_z^{(b2)} \right) n_{(i)}^{(b2)} / n_z^{(b2)} \right) = 0 \\ \text{on } S_{B2}, \end{array} \right. \quad (40)$$

405 where $\tau_{(i)j}^{BP}$ is given by (37).

406 (2) Variation with respect to w yields the vertical momentum equation:

$$407 \quad -\frac{\partial \tilde{P}}{\partial z} = 0; \quad \tilde{P} n_z^{(s)} = 0 \text{ on } S_S, \quad (41)$$

408 (3) Variation with respect to \tilde{P} yields the continuity equation:

$$409 \quad \frac{\partial w}{\partial z} + \frac{\partial u_{(i)}}{\partial x_{(i)}} = 0; \quad w = 0 \text{ on } S_{B1}, \text{ or } w = -u_{(i)} n_{(i)}^{(b2)} / n_z^{(b2)} \text{ on } S_{B2}. \quad (42)$$

410 This appears to be a coupled system for the complete set of variables, u, v, w, \tilde{P} , just as in
 411 the transformed Stokes model. However, it is apparent that the vertical momentum
 412 equation system (41) is decoupled and results in $\tilde{P} = 0$, as was already shown in §3.1.
 413 This eliminates pressure from the horizontal momentum equation (40), making it
 414 identical to the standard Blatter-Pattyn system (36). Finally, having obtained the
 415 horizontal velocities from the solution of (40), the continuity equation (42) may be solved
 416 for the vertical velocity component w (but see the comments regarding the discrete case
 417 that follow (43)).

418

419 In summary, the extended Blatter-Pattyn model, (40)-(42), is equivalent to the
 420 standard Blatter-Pattyn model, (36), for the horizontal velocities, u, v , except that it also
 421 includes two additional equations that determine the pressure \tilde{P} and the vertical velocity
 422 w , which are usually ignored in the standard Blatter-Pattyn approximation when only the
 423 horizontal velocity is of interest. Because of this, we distinguish between the *Blatter-*
 424 *Pattyn model* that solves for just the two horizontal velocities (i.e., the standard Blatter-
 425 Pattyn approximation, (36)), and the *Blatter-Pattyn system* that solves for all the variables
 426 (i.e., the extended Blatter-Pattyn approximation, (40)-(42)). It may not be obvious why
 427 we wish to deal with the extended Blatter-Pattyn system since we already know that it is
 428 equivalent to the simpler Blatter-Pattyn model. As it turns out, the Blatter-Pattyn system
 429 is needed for future applications, to be described in §6, because it allows for a dual-model

430 code and for easy switching between the Blatter-Pattyn and Stokes models, which may be
431 a useful feature in a general ice sheet code (e.g., ISSM, Larour et al., 2012), and because
432 it also enables an adaptive hybrid scheme where the cheaper Blatter-Pattyn
433 approximation is used locally within a Stokes model.

434

435 To complete the solution of the Blatter-Pattyn system once pressure \tilde{P} and the
436 horizontal velocities u, v are available, the continuity equation (42) needs to be solved for
437 the vertical velocity w . The use of the continuity equation to solve for the vertical
438 velocity w is a novel feature of the Blatter-Pattyn approximation since the continuity
439 equation is not normally used for this purpose. Using Leibniz's theorem, the continuity
440 equation may be integrated starting from the bottom to obtain the vertical velocity in
441 terms of horizontal velocity components, as follows

442
$$w(u, v) = w_{z=z_b} - \int_{z_b}^z \frac{\partial u_{(i)}}{\partial x_{(i)}} dz' = u_{(i)} \frac{\partial z_b}{\partial x_{(i)}} - \int_{z_b}^z \frac{\partial u_{(i)}}{\partial x_{(i)}} dz' = - \frac{\partial}{\partial x_{(i)}} \int_{z_b}^z u_{(i)} dz'. \quad (43)$$

443 Note that we have replaced $w_{z=z_b}$ by $u_{(i)} \partial z_b / \partial x_{(i)}$. This is valid for either of the basal
444 boundary conditions (9) or (10) (here (10) is in the form given by (14)). When solving
445 the Blatter-Pattyn system, the right-hand-side is known. However, (43) also works
446 symbolically when the horizontal velocities $u_{(i)}$ are not yet known, and therefore $w(u, v)$
447 is a functional of the unknown horizontal velocity distribution.

448

449 Thus far, we have only considered continuum results. A discrete finite element
450 formulation, however, may not be well behaved. The solution of the discretized Stokes
451 models and the associated Blatter-Pattyn approximations, and the ability to solve for the
452 vertical velocity as in (43), will depend on the choices made for the grids and for the
453 finite elements that are to be used. These issues will be discussed next.

454

455 **4. Finite Element Discretization**

456 **4.1 Standard and Transformed Stokes Discretizations**

457

458 In practice, both traditional Stokes and Blatter-Pattyn models are discretized using finite
459 element methods (e.g., Gagliardini et al., 2013; Perego et al., 2012). We follow this
460 practice except that here the discretization originates from a variational principle. This
461 has a number of advantages (see §2.3 and DPL, 2010). The following is a brief outline of
462 the finite element discretization. Additional details about the grid and the associated



463 discretization are provided in Appendix C. For simplicity, we confine ourselves to two
 464 dimensions with coordinates (x, z) and velocities (u, w) . Generalization to three
 465 dimensions should be clear (an example of a three-dimensional grid appropriate for our
 466 purpose is discussed in Appendix C). Further, we present only the simpler case of direct
 467 substitution for the basal boundary conditions in the variational functional, i.e., (15) or
 468 (33). The remarks in this Section apply to both the standard and transformed Stokes
 469 models; for example, the discrete pressure variable p may refer to either the standard
 470 pressure P or the transformed pressure \tilde{P} .

471

472 Consider an arbitrary grid with a total of $N = n_u + n_w + n_p$ unknown discrete
 473 variables at appropriate nodal locations $1 \leq i \leq N$, with n_u horizontal velocity variables,
 474 n_w vertical velocity variables, and n_p pressure variables, such that

475
$$U = \{U_1, U_2, \dots, U_N\}^T = \left\{ \left\{ u_1, u_2, \dots, u_{n_u} \right\}, \left\{ w_1, w_2, \dots, w_{n_w} \right\}, \left\{ p_1, p_2, \dots, p_{n_p} \right\} \right\}^T = \{u, w, p\}^T \quad (44)$$

476 is the vector containing all the unknown discrete variables. These are the degrees of
 477 freedom of the model. If using Lagrange multipliers for basal boundary conditions then
 478 discrete variables corresponding to λ_2, Λ must be added. Variables are expanded in

479 terms of shape functions $N_i^k(\mathbf{x})$ associated with each nodal variable i in each element

480 k , such that $U^k(\mathbf{x}) = \sum_i U_i N_i^k(\mathbf{x})$ is the spatial variation of all the variables in element

481 k . The summation is over all variable nodes located in element k . Shape functions

482 associated with a given node may differ depending on the variable (i.e., u, w , or p).

483 Substituting into the functional, (15) or (33), integrating and assembling the contributions

484 of all elements, we obtain a discretized variational functional in terms of the nodal

485 variable vectors u, w, p , as follows

486
$$\mathcal{A}(u, w, p) = \sum_k \mathcal{A}^k(u, w, p), \quad (45)$$

487 where $\mathcal{A}^k(u, w, p)$ is the local functional evaluated by integrating over element k . Since

488 the term in the functional involving the product of pressure and divergence of velocity is

489 linear in pressure and velocity, and the term responsible for gravity forcing is linear in

490 velocity, the functional (45) may be written in matrix form as follows

491
$$\mathcal{A}(u, w, p) = \mathcal{M}(u, w) + p^T \left(M_{UP}^T u + M_{WP}^T w \right) + u^T F_U + w^T F_W, \quad (46)$$



492 where the shorthand notation from (44) is used, i.e., $u = \{u_1, u_2, \dots, u_{n_u}\}^T$, etc. Parentheses
 493 indicate a functional dependence on the indicated variables. Comparison with (15) and
 494 (33) indicates that $\mathcal{M}(u, w)$ is a nonlinear positive-definite function of the velocity
 495 components u, w , M_{UP}, M_{WP} are constant $n_u \times n_p$ and $n_w \times n_p$ matrices, respectively,
 496 arising from the incompressibility constraint in the functional, and F_U, F_W are constant
 497 gravity forcing vectors, of dimension n_u and n_w , respectively. Note that $F_U = 0, F_W \neq 0$
 498 in the standard Stokes model and $F_U \neq 0, F_W = 0$ in the transformed Stokes model. The
 499 discrete functional $\mathcal{M}(u, w)$ differs in the two models but it remains positive-definite in
 500 both, which has important consequences, as will be seen in Appendix D.

501

502 Discrete variation of the functional corresponds to partial differentiation with
 503 respect to each of the discrete variables in U . Thus, the discrete Euler-Lagrange
 504 equations that correspond to the u-momentum, w-momentum, and continuity equations,
 505 respectively, are given by

$$506 \quad R(u, w, p) = \begin{bmatrix} R_U(u, w, p) \\ R_W(u, w, p) \\ R_p(u, w) \end{bmatrix} = \begin{bmatrix} \mathcal{M}_U(u, w) + M_{UP}p + F_U \\ \mathcal{M}_W(u, w) + M_{WP}p + F_W \\ M_{UP}^T u + M_{WP}^T w \end{bmatrix} = 0, \quad (47)$$

507 where $R(u, w, p)$ is the residual vector (actually, it is the negative of the usual definition
 508 of the residual) with components $R_U(u, w, p) = \partial \mathcal{A} / \partial u$, $R_W(u, w, p) = \partial \mathcal{A} / \partial w$, and
 509 $R_p(u, w) = \partial \mathcal{A} / \partial p$. The functionals $\mathcal{M}_U(u, w) = \partial \mathcal{M} / \partial u$, $\mathcal{M}_W(u, w) = \partial \mathcal{M} / \partial w$ are
 510 nonlinear vectors of dimension n_u and n_w , respectively. Altogether, (47) is a set of N
 511 equations for the N unknown discrete variables U_i . As explained previously, all
 512 boundary conditions are already included in functional (46), and therefore are also
 513 included in the discrete Euler-Lagrange equations (47).

514

515 Since the overall system (47) is nonlinear, it is typically solved using Newton-
 516 Raphson iteration, expressed in matrix notation as follows

$$517 \quad M(u^K, w^K) \Delta U^{K+1} + R(u^K, w^K, p^K) = 0, \quad (48)$$



518 where K is the iteration index, $M(u, w) = \partial^2 \mathcal{A}(U) / \partial U_i \partial U_j$ is a symmetric $N \times N$

519 Hessian matrix, and Δ^{K+1} is the column vector given by

520
$$\Delta U^{K+1} = [u^{K+1} - u^K, w^{K+1} - w^K, p^{K+1} - p^K]^T.$$

521 Given U_i^K from the previous iteration, (48) is a linear matrix equation that is solved for

522 the N new variables U_i^{K+1} at each iteration. In view of (46) and (47), the Hessian matrix

523 $M(u, w)$ may be decomposed into several submatrices, as follows

524
$$M(u, w) = \begin{bmatrix} M_{UU}(u, w) & M_{UW}(u, w) & M_{UP} \\ M_{UW}^T(u, w) & M_{WW}(u, w) & M_{WP} \\ M_{UP}^T & M_{WP}^T & 0 \end{bmatrix}. \quad (49)$$

525 Submatrices $M_{UW}(u, w) = \partial^2 \mathcal{M} / \partial u \partial w$, etc., depend nonlinearly on u, w . Thus,

526 $M_{UU}(u, w), M_{WW}(u, w)$ are square $n_u \times n_u, n_w \times n_w$ matrices, respectively, while

527 $M_{UW}(u, w)$ is a rectangular $n_u \times n_w$ matrix since n_u, n_w may not be equal. As noted

528 earlier, M_{WP} is a $n_w \times n_p$ matrix and therefore not square unless $n_p = n_w$. Additionally,

529 $M_{UU}(u, w)$ and $M_{WW}(u, w)$ are symmetric by definition.

530

531 **4.2 Blatter-Pattyn Discretizations**

532

533 For completeness, we express the Blatter-Pattyn approximations from §3.4 in matrix

534 form, as follows

535 (1) The standard Blatter-Pattyn model from §3.4.1 takes the simple form

536
$$R^{BP}(u) = \mathcal{M}_U(u, 0) + F_U = 0, \quad (50)$$

537 with the corresponding Newton-Raphson iteration given by

538
$$M^{BP}(u^K) \Delta u^{K+1} + R^{BP}(u^K) = 0, \quad (51)$$

539 where the Blatter-Pattyn Hessian matrix is $M^{BP}(u) = M_{UU}(u, 0)$.



540 (2) The extended Blatter-Pattyn approximation from §3.4.2 becomes

$$541 \quad R^{EBP}(u, w, p) = \begin{bmatrix} \mathcal{M}_U(u, 0) + M_{UP}p + F_U \\ M_{WP}p \\ M_{UP}^T u + M_{WP}^T w \end{bmatrix} = 0, \quad (52)$$

542 and the Newton-Raphson iteration is given by

$$543 \quad M^{EBP}(u^K) \Delta U^{K+1} + R^{EBP}(u^K, w^K, p^K) = 0, \quad (53)$$

544 where the associated Hessian matrix is

$$545 \quad M^{EBP}(u) = \begin{bmatrix} M_{UU}(u, 0) & 0 & M_{UP} \\ 0 & 0 & M_{WP} \\ M_{UP}^T & M_{WP}^T & 0 \end{bmatrix}. \quad (54)$$

546

547 4.3 Solvability Issues

548

549 We now consider the solution of the three linear matrix problems (48), (51), (53). While
550 there is no issue in the continuous case, there may be problems in the discrete case
551 depending on the choice of the grid and the finite elements, as noted earlier.

552

553 4.3.1 Solvability of the Standard and Transformed Stokes Models

554

555 The Hessian matrix in the standard and transformed Stokes cases, (49), has the form

$$556 \quad M(u, w) = \begin{bmatrix} A & B \\ B^T & 0 \end{bmatrix}, \quad (55)$$

557 where

$$558 \quad A = A^T = \begin{bmatrix} M_{UU}(u, w) & M_{UW}(u, w) \\ M_{UW}^T(u, w) & M_{WW}(u, w) \end{bmatrix}, \quad B = \begin{bmatrix} M_{UP} \\ M_{WP} \end{bmatrix}, \quad B^T = \begin{bmatrix} M_{UP}^T & M_{WP}^T \end{bmatrix}.$$

559 The general form (55) is characteristic of Stokes-type problems, or more generally, of
560 constrained minimization problems using Lagrange multipliers. In finite element
561 terminology these are “mixed” problems, meaning that velocity components and the
562 pressure occupy different finite element spaces, or else they are “saddle point” problems

563 since the Hessian matrix $M(u, w)$ is symmetric but indefinite, with both positive and



564 negative eigenvalues. This can give rise to solution instabilities. To avoid this, elements
565 that are to be used must satisfy the so-called inf-sup or LBB condition constraining the
566 matrix B in (55). There is a very large literature on the subject, e.g., Elman et al. (2014).
567 Testing for stability is not trivial. Both the standard and transformed Stokes models are
568 subject to these issues and in general must use inf-sup-stable finite elements. An
569 example of an inf-sup stable element is the popular second-order Taylor-Hood P2-P1
570 element with piecewise quadratic velocity and linear pressure (Hood and Taylor, 1973).
571 Both the standard and transformed Stokes models are stable using the Taylor-Hood
572 element. Some results involving the Taylor-Hood element are shown in Fig. 13 for Test
573 B, one of the test problems described in Appendix B that corresponds to Exp. B from the
574 ISMIP–HOM model intercomparison (Pattyn et al., 2008).

575

576 **4.3.2 Solvability of the Standard Blatter-Pattyn Model**

577

578 The standard Blatter-Pattyn approximation is not subject to these stability issues since
579 pressure, the Lagrangian multiplier, is absent in (51). As a result, the standard Blatter-
580 Pattyn variational formulation (34) is actually a well-behaved and stable positive-definite
581 minimization or optimization problem.

582

583 **4.3.3 Solvability of the Extended Blatter-Pattyn Model**

584

585 We noted earlier that the transformed Stokes model works well using the Taylor-Hood
586 element in Test B. Since the extended Blatter-Pattyn model has the same structure as the
587 transformed full-Stokes model and yields the same solution for horizontal velocity as the
588 standard Blatter-Pattyn model, one might expect its discrete implementation to behave
589 well. However, the extended Blatter-Pattyn model fails badly in this problem, with
590 nonsensical results for the vertical velocity. This may be because there is an additional
591 requirement for the stability of a Stokes-type problem that is not met in this case, namely,
592 the matrix A in (55) must be elliptic on the whole u, w space (Auricchio et al., 2017).
593 However, there is a much simpler explanation. Consider the vertical momentum
594 equation, the second of the extended Blatter-Pattyn model equations from (52). As is
595 seen in §3.4.2 or from the second of the equations in (52) in the extended Blatter-Pattyn
596 approximation, this equation is a decoupled linear system for the pressure. Since the
597 equation involves the M_{wp} matrix, we have a decoupled set of n_w equations that needs to

598 be solved for the n_p pressure variables. This is not possible unless the matrix M_{wp} is
599 square. For the same reason, the third of the equations in (52) cannot be solved for w
600 unless matrix M_{wp}^T is invertible. In other words, the extended Blatter-Pattyn model (52)
601 only works when $n_w = n_p$, which is not the case in a Taylor-Hood discretization. This is
602 because in finite element discretizations of Stokes problems, the pressure approximation
603 is typically one degree lower than the velocity approximation, which leads to fewer
604 pressure variables than velocity variables. In the case of the Taylor-Hood element, the
605 difference is very large and we have $n_w \gg n_p$ (see §7 for more details). This means that
606 in the extended Blatter-Pattyn model vertical velocity is greatly underdetermined, which
607 accounts the problem in the Taylor-Hood calculation. This problem also manifests itself
608 in Taylor-Hood discretizations of Stokes models but to a much lesser extent. For
609 example, mass is poorly conserved in the Taylor-Hood discretization of the standard
610 Stokes model (Boffi et al., 2012). In the transformed Stokes case there tend to be
611 velocity oscillations that tend to go away when using a grid in which $n_p = n_w$ (see Fig. 13,
612 Panels E and F).

613

614 **4.3.4 The Solvability Condition**

615

616 Summarizing, the extended Blatter-Pattyn approximation is problematic unless we have

$$617 \quad n_p = n_w. \quad (56)$$

618 In addition, the resulting square matrix M_{wp} must be non-singular, which we assume to be
619 the case for a reasonable finite element discretization. This makes it possible to solve for
620 the pressure in the extended Blatter-Pattyn system (52) because M_{wp} is square and
621 invertible. We henceforth refer to (56), together with non-singularity, as the solvability
622 condition for the pressure. This is a characteristic or a property associated with the
623 discrete grid and the boundary conditions. In Appendix C, we consider several grids that
624 exhibit this property. The specific solvability condition given by (56) applies when direct
625 substitution is used for basal boundary conditions. The number of unknown pressures n_p
626 must be augmented if Lagrange multipliers are used and (56) becomes $n_p + \lambda_z + \Lambda = n_w$
627 (See Appendix C, §C2).

628



629 The solvability condition has an additional implication. If matrix M_{WP} is square
 630 and invertible due to (56), then its transpose M_{WP}^T is also square and invertible. This
 631 implies that the continuity equation in (47) and (52), that is,

$$632 \quad M_{UP}^T \mathbf{u} + M_{WP}^T w = 0, \quad (57)$$

633 is solvable for the vertical velocity w in terms of the horizontal velocities, as follows

$$634 \quad w(\mathbf{u}) = -M_{WP}^{-T} M_{UP}^T \mathbf{u}, \quad (58)$$

635 where the matrix M_{WP}^{-T} is defined by

$$636 \quad M_{WP}^{-T} = \left(M_{WP}^T \right)^{-1} = \left(M_{WP}^{-1} \right)^T. \quad (59)$$

637 Note that (58) is the discrete form of equation (43). Thus, since the invertibility of M_{WP}
 638 implies the invertibility of M_{WP}^T , the solvability condition (56) implies the solvability of
 639 the continuity equation (58), and vice-versa. As we shall see, this property is not just a
 640 useful property but it is necessary for the new Stokes approximations that improve on the
 641 Blatter-Pattyn approximation, as discussed in §6.2.

642
 643 Perhaps the main reason for the importance of the solvability condition is
 644 demonstrated in Appendix D. Appendix D shows that a variational principle that
 645 complies with the solvability condition is equivalent to an optimization or minimization
 646 problem, which is sufficient for the stability of the corresponding Stokes model. Thus,
 647 for example, the extended Blatter-Pattyn model fails with a Taylor-Hood P2-P1 grid,
 648 which does not satisfy the solvability condition, but works well with a variant, the P2-E1
 649 grid, shown in Fig. 13A, that does satisfy the solvability condition. Several finite
 650 elements that satisfy the condition are presented in Appendix C. One particular element,
 651 the P1-E0 element, is particularly useful for use with the transformed Stokes model
 652 because the solvability condition is satisfied locally, i.e., along individual vertical grid
 653 lines, as shown in Appendix C. This element is used in most of the 2D test problems
 654 featured here.

655

656 **5. Comparison of the Standard and Transformed Stokes Models**

657

658 To compare the standard and transformed Stokes models we use two 2D test problems,
 659 namely, Exp. B from the ISMIP-HOM benchmark (Pattyn et al, 2008), and Exp. D*, a
 660 modified version of Exp. D from the ISMIP-HOM suite. A description of these tests is



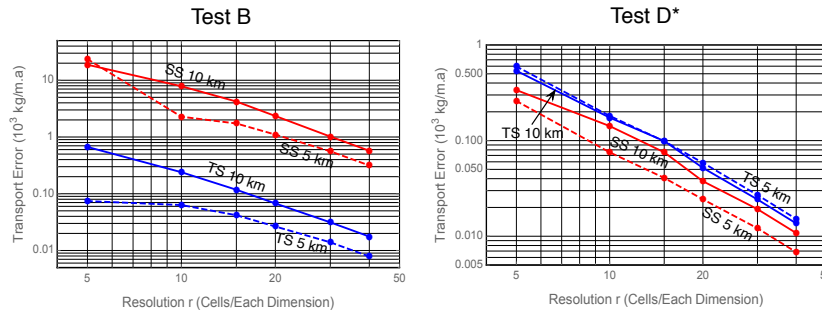
661 provided in Appendix B, where they are referred to as Test B and Test D*. Test B
662 involves no-slip boundary conditions on a sinusoidal bed, and Test D* evaluates sliding
663 of the ice sheet along a flat bed in the presence of sinusoidal friction. The tests are
664 discretized using P1-E0 elements on a regular grid composed of n quadrilaterals in the
665 x -direction and m quadrilaterals in the z -direction, with each quadrilateral divided into
666 two triangles as illustrated in Figs. C3 and described in Appendix D. The results
667 presented in this Section are for a relatively coarse 40x40 grid, i.e., $m = n = 40$, except
668 when we consider the convergence of the models with grid refinement.

670 **5.1 Convergence of Solutions with Grid Refinement**

671
672 We first look at the convergence of the transformed and standard Stokes models as the
673 grid is refined in Fig. 3. In particular, we look at the convergence of ice transport through
674 a vertical cross section of the ice sheet at $x = L$. The ice transport T is defined by

$$675 \quad T = \int_{z_b}^{z_s} u(L, z) dz, \quad (60)$$

676 where the vertical profile $u(L, z)$ is plotted in Fig. 4 for several cases at the 40x40
677 resolution. Fig. 3 plots the absolute value of the transport error $E = ||T - T_R||$ as a function
678 of the resolution r , where r is the number of quadrilaterals in either direction (since
679 $r = m = n$) and T_R is the converged value of the transport obtained by Richardson
680 extrapolation using the two highest resolution values. The transport is evaluated at
681 various resolutions $r = 5, 10, 15, 20, 30, 40$, and plotted at two domain lengths, $L = 5$ and
682 10 km. Trying to estimate the rate of convergence in this way is highly uncertain, as
683 discussed in §7, but estimating the error is a more reasonable thing to do. Both models
684 are consistent with second order convergence, as expected from the use of linear
685 elements, but they behave quite differently in the two test problems. The transformed
686 Stokes model (TS) is some two orders of magnitude more accurate at all resolutions than
687 the standard Stokes model (SS) in Test B calculations although they start from the same
688 initial conditions. However, the accuracy of the two models is quite similar in Test D*
689 calculations, with the SS error actually somewhat smaller than the TS error. This is
690 confirmed when we compare the details of the u -velocity solutions in Figs. 4 and 5 at the
691 40x40 resolution. The TS and SS profiles differ noticeably from each other but are quite
692 similar in the Test D* case. However, the standard and transformed Stokes models do
693 eventually converge to the same solution.



694

695

Figure 3. Convergence of ice transport in Tests B and D* with grid refinement.

696

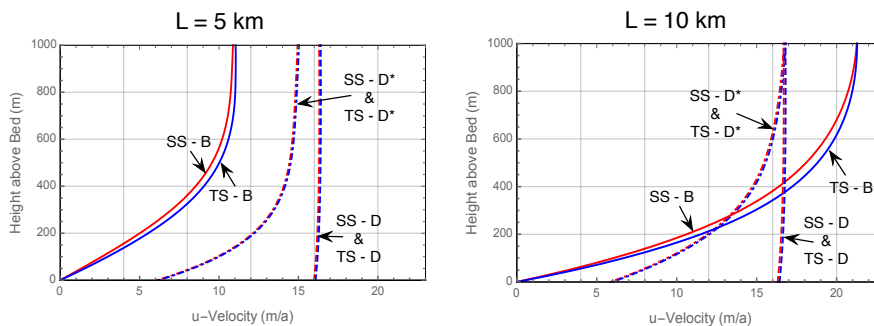
Transformed Stokes plots are in blue and standard Stokes plots are in red.

697

698 5.2 The Vertical Profile of Solutions

699

700 Fig. 4 shows the vertical profiles of the horizontal velocity u at $x = L$ for the 40x40
 701 resolution in the transformed and standard Stokes models. There is a noticeable
 702 difference in the two profiles in Test B, as is to be expected from Fig. 3 results where we
 703 see that the SS calculation is not yet as well converged as the TS case at this resolution.
 704 Also shown in Fig. 4 are profiles from the two frictional sliding problems, Tests D and
 705 D*. The Test D profile, i.e., Exp. D from the ISMIP-HOM benchmark, is almost
 706 vertically constant, indicating that the originally chosen value for basal friction is too
 707 small, i.e., more appropriate for a shallow-shelf approximation. This motivated the
 708 modification of Test D to Test D*, as described in Appendix B. In contrast to the Test B
 709 case, the standard and transformed frictional Test D and D* plots cannot be visually
 710 distinguished from each other, as might be expected from the similar error convergence
 711 for the Test D* results in Fig. 3.



712

713

Figure 4. The u -velocity profile at location $x = L$ as a function of height from the bed.

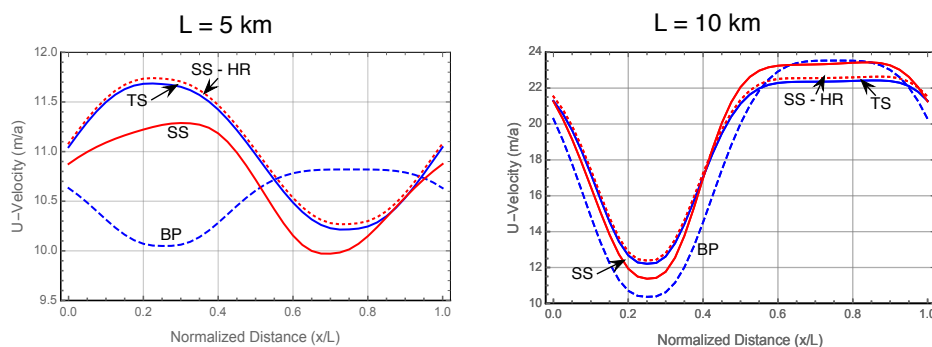
714



715 **5.3 The Upper Surface Horizontal Velocity**

716

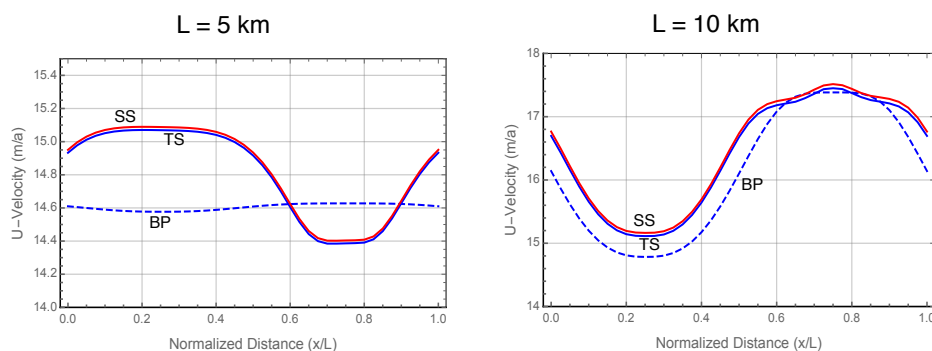
717 Figs. 5 and 6 show the u -velocity at the upper surface at the 40×40 resolution for Tests B
 718 and D^* , respectively. This is the basic benchmark used in ISMIP-HOM to compare the
 719 different ice sheet models. Here we compare four cases: the standard Stokes model (SS),
 720 the transformed Stokes model (TS), the Blatter-Pattyn (BP) model, and for reference, the
 721 very high resolution full-Stokes calculation “oga1” presented in the ISMIP-HOM paper
 722 (SS-HR). The SS-HR calculation is also available independently in Gagliardini and
 723 Zwinger (2008). Results are presented for two domain lengths, $L = 5$ km and 10 km, to
 724 observe the behavior of the SS and TS models in the aspect ratio range where the Blatter-
 725 Pattyn model begins to fail.



726

727 **Figure 5.** Upper surface u -velocity, $u(x, z_s)$ - Test B, No-slip boundary conditions.

728



729

730 **Figure 6.** Upper surface u -velocity, $u(x, z_s)$ - Test D^* , Modified frictional sliding case.

731

732 The TS and the SS-HR plots in Fig. 5 lie on top of one another (the SS-HR plot
 733 (dotted) has been slightly offset upward for clarity), indicating that the transformed



734 Stokes model is already fully converged, and confirming that the standard and
735 transformed Stokes models do indeed converge to the correct Stokes solution. We again
736 observe that the SS results are not yet converged in Test B at this resolution, particularly
737 at $L = 5$ km. As also seen in the ISMIP-HOM benchmark paper, the Blatter-Pattyn
738 calculation (BP) shows large deviations from the Stokes results, especially so at $L = 5$
739 km where surface velocity is entirely out of phase with the Stokes results. Test D*
740 frictional sliding results follow a similar pattern in Fig. 6. Since convergence of the SS
741 and TS models is very similar in the frictional case, the SS and TS plots overlies one
742 another (the SS plot has been slightly offset upward for visibility), confirming that the
743 two Stokes models converge to the same solution. As was seen in Test B, the Blatter-
744 Pattyn error is quite large at $L = 10$ km, and dramatically so at $L = 5$ km.

745

746 **6. Some Applications of the Transformed Stokes Model**

747 **6.1 Adaptive Switching between Stokes and Blatter-Pattyn Models**

748

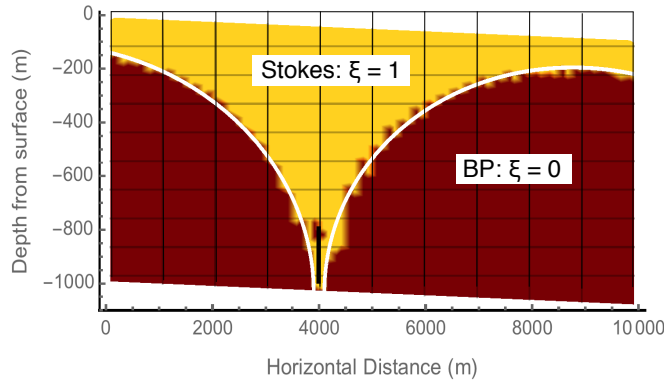
749 One way of reducing the cost of a full Stokes calculation is to use it adaptively with a
750 cheaper approximate model in a given problem. That is, one may use the cheaper model
751 in those parts of a problem where it is accurate, and the more expensive full Stokes model
752 where the approximate model loses accuracy. One example of such an adaptive approach
753 is the tiling method by Seroussi et al. (2012). However, there are drawbacks to such
754 methods, such as the difficulty of incorporating two or more presumably quite different
755 models into a single model, and the additional complexity of a transition zone in order to
756 couple the disparate models.

757

758 Using the transformed Stokes model in such an adaptive role is attractive because
759 it may be switched between the Stokes and Blatter-Pattyn cases simply by switching the
760 parameter $\xi \in \{0,1\}$ between its two values. To avoid complications and more difficult
761 programming it is essential that both the Stokes and the Blatter-Pattyn parts of the code
762 have the same number of discrete variables. This implies that the extended Blatter-Pattyn
763 approximation ($\hat{\xi} = 1$) must be used, which therefore implies the use of a grid that
764 satisfies the solvability condition for reasons discussed in §4 and Appendix C. To do
765 this, we will discretize using the P1-E0 element. To demonstrate the idea of adaptive
766 switching with a transformed Stokes model, we introduce a new test problem, Test O,
767 described in Appendix B and illustrated in Fig. B1. This consists of an inclined ice slab
768 whose movement is obstructed by a thin obstacle protruding 20% of the ice depth up



769 from the bed. No-slip boundary conditions are applied along the bed and on the obstacle
 770 itself. Because of the localized nature of the obstacle, the conditions for the Blatter-
 771 Pattyn approximation to be valid, (38), must fail near the obstacle and therefore the full
 772 Stokes model is needed for good accuracy, at least locally.



773

774 **Figure 7.** Mask function (white curve, $z = F_M(x)$) to indicate where the Stokes and BP
 775 models are activated in the adaptive hybrid 20% obstacle test problem. The dark brown
 776 region delineates the region where $|\partial w/\partial x| \leq 0.1|\partial u/\partial z|$ in a Blatter-Pattyn calculation.

777

778 To implement this idea, we first use a Blatter-Pattyn calculation to outline regions
 779 where $|\partial w/\partial x| \leq 0.1|\partial u/\partial z|$, approximately localizing where the Blatter-Pattyn

780 approximation is valid. This determines a mask function $z = F_M(x)$, illustrated in Fig. 7

781 by the two white curves, that specifies where the two models must be used. Defining the

782 centroid of a triangular element by (x_c, z_c) , the code makes the following selection in

783 each element,

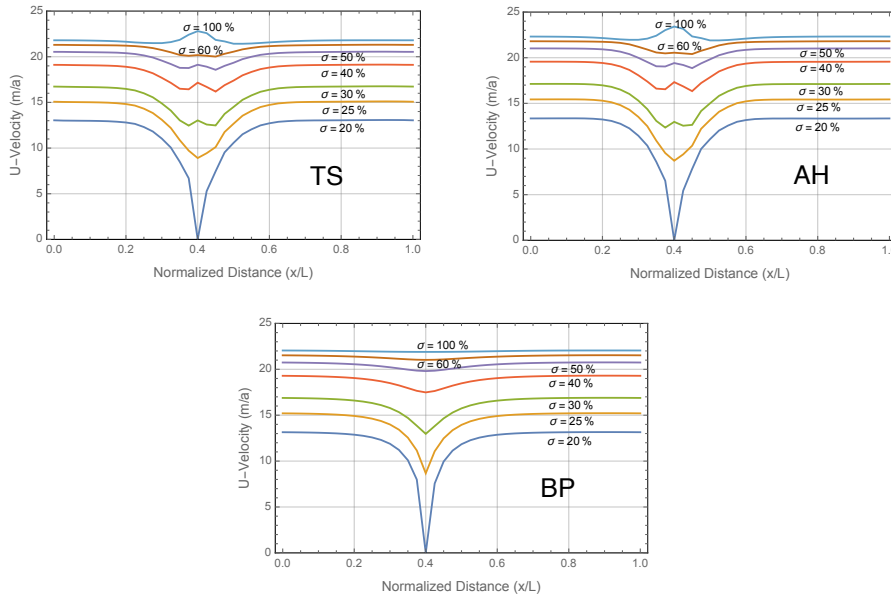
784 $z_c \leq F_M(x_c) \Rightarrow$ Set $\xi = 0$, i.e., the Blatter-Pattyn region,

$z_c > F_M(x_c) \Rightarrow$ Set $\xi = 1$, i.e., the Stokes region.

785 Somewhat counterintuitively, the Stokes region occupies the upper part of the domain in
 786 Fig. 7 and includes the obstacle, while the Blatter-Pattyn region occupies much of the
 787 bottom part of the domain. It would be possible to introduce a transition zone, e.g.,

788 $0 \leq \xi(x, z) \leq 1$, but this was not deemed necessary and it was not done in the present

789 calculation.



790

791

792

793

794

795

796

797

798

799

800

801

802

803

804

805

806

807

808

809

Figure 8. Comparing results for the Transformed Stokes (TS, i.e., the exact Stokes), the Adaptive-Hybrid (AH), and the Blatter-Pattyn (BP) models for Test O.

The Adaptive-Hybrid results are shown in Fig. 8, which shows curves of the horizontal velocity u at seven different vertical positions specified as a percentage of the distance between top and bottom, such that $\sigma = 100\%$ is at the top surface. The top right panel shows the results for the adaptive-hybrid model. For comparison, the top left panel and the bottom panel show results for the full Stokes and the Blatter-Pattyn calculations, respectively. All calculations are at the 40×40 resolution. The Adaptive-Hybrid results are very similar to the full Stokes results, reproducing most features of the velocity profiles, including the velocity bump at the top surface, indicating that even the top surface feels the presence of the obstacle. The Blatter-Pattyn results are much less accurate; they completely miss the details of the flow near the obstacle. We also calculate a measure of the error relative to the transformed Stokes results, the overall RMS u-Error, defined as follows

$$\text{RMS u-Error} = \sqrt{\sum_{k=1}^{n_u} (u_k - u_k^{TS})^2 / n_u}, \quad (61)$$

where u_k^{TS} is the transformed Stokes horizontal velocity discrete variable. The overall RMS u-Error in the Blatter-Pattyn case is 0.493 m/a while the Adaptive-Hybrid error is 0.440 m/a, smaller in the Blatter-Pattyn case, as expected, but the difference is not big



810 and not as striking as the visual differences in Fig. 8. Nevertheless, the adaptive-hybrid
811 method can be judged successful by the results presented in Fig. 8 alone. Unfortunately,
812 a reasonable estimate of the computational cost savings cannot be made because of the
813 small-scale nature of these calculations that were carried out on a personal computer.

814

815 **6.2. Two Stokes Approximations Beyond Blatter-Pattyn**

816

817 As shown in §3.4, simply setting $w=0$ in the second invariant $\tilde{\epsilon}^2$ in the transformed
818 functional $\tilde{\mathcal{A}}$, given by (28) and (33), respectively, results in the Blatter-Pattyn system of
819 equations. This suggests that approximating the vertical velocity w in the transformed
820 functional would be a good way to create approximations that improve on the Blatter-
821 Pattyn approximation since providing no information at all, i.e., $w=0$, already produces
822 an excellent approximation. We will look at only two such methods in this Section even
823 though many other variations are possible. The first method, to be called the BP+
824 approximation, improves the Blatter-Pattyn approximation simply by using a lagged
825 value of the vertical velocity in the functional (33). It is implemented using a
826 combination of Newton and Picard iterations such that at each Newton iteration the
827 variational functional is evaluated using the known vertical velocity w^K from the
828 previous iteration, where K is the iteration index. The vertical velocity, $w^K = w(u^K)$, is
829 obtained by using (58) together with a grid that is consistent with an invertible continuity
830 equation, such as the P1-E0 grid from Appendix C. The second method, to be called the
831 Dual-Grid approximation, approximates the transformed Stokes model by discretizing the
832 continuity equation on a coarser grid. Since vertical velocity w is to be determined by
833 inverting the continuity equation, this has the effect of approximating the vertical velocity
834 while at the same time reducing the number of pressure and vertical velocity variables.
835 The degree of grid coarsening determines the accuracy of the resulting approximation.

836

837 **6.2.1 An Improved Blatter-Pattyn or BP+ Approximation**

838

839 To prepare, we introduce a pair of 2D variational quasi-functionals, $\tilde{\mathcal{A}}_{PS1}[u, w]$ and
840 $\tilde{\mathcal{A}}_{PS2}[\tilde{P}]$. Noting that $\tilde{P}=0$ in the Blatter-Pattyn approximation, we drop the pressure
841 term from the transformed functional (33) and define a new functional,



$$\begin{aligned} \tilde{\mathcal{A}}_{PS1}[u, w] = & \int_V dV \left[\frac{4n}{n+1} \eta_0 (\tilde{\varepsilon}^2)^{(1+n)/2n} + \rho g u \frac{\partial z_s}{\partial x} \right] \\ & + \frac{1}{2} \int_{S_{B2}} dS \beta(x) \left(u^2 + \zeta \left(u n_x^{(b2)} / n_z^{(b2)} \right)^2 \right), \end{aligned} \quad (62)$$

843 where

$$\tilde{\varepsilon}^2 = \left(\frac{\partial u}{\partial x} \right)^2 + \frac{1}{4} \left(\frac{\partial u}{\partial z} + \frac{\partial w}{\partial x} \right)^2. \quad (63)$$

845 Since the continuity equation has been eliminated, we introduce incompressibility
846 separately by defining another functional,

$$\tilde{\mathcal{A}}_{PS2}[p] = \int_V dV p \left(\frac{\partial u}{\partial x} + \frac{\partial w}{\partial z} \right). \quad (64)$$

848 Since direct substitution is used for boundary conditions, then (9) and (14) are the
849 appropriate basal boundary conditions needed to specify w in (64); no boundary
850 condition is required for the pressure. Here we are effectively viewing the pressure p as
851 a “test function” in the finite element sense. This gives us great flexibility to create
852 elements that satisfy the solvability condition (56). In a triangulation, for example, some
853 pressures may be assigned to every two triangles, as in a P1-E0 grid, while others may be
854 assigned to a single triangle to achieve an equal number of pressure and vertical velocity
855 variables.

856

857 The discrete variation of $\tilde{\mathcal{A}}_{PS1}[u, w]$ with respect to u , results in a set of n_u Euler-
858 Lagrange equations,

$$\hat{R}_U(u, w) = \frac{\partial \tilde{\mathcal{A}}_{PS1}(u, w)}{\partial u} = M_U(u, w) + F_U = 0. \quad (65)$$

860 This may be recognized as the standard Blatter-Pattyn model, (50), when $w = 0$. The

861 discrete variation of $\tilde{\mathcal{A}}_{PS2}[p]$ with respect to p , results in the continuity equation, (57),

$$\hat{R}_p(u, w) = \frac{\partial \tilde{\mathcal{A}}_{PS2}(p)}{\partial p} = M_{UP}^T u + M_{WP}^T w = 0. \quad (66)$$

863 These two systems are now combined to form the BP+ approximation, as follows

$$\hat{R}(u, w) = \left[\hat{R}_U(u, w), \hat{R}_p(u, w) \right]^T = 0. \quad (67)$$

865 This is a single system of $n_u + n_p$ equations to determine the $n_u + n_w$ discrete velocities

866 u, w , implying that (67) is viable only on grids satisfying the solvability condition,



867 $n_p = n_w$. Just as in the standard Blatter-Pattyn approximation in §3.4.1, the vertical
 868 momentum equation is missing, but instead of neglecting w , the vertical velocity is now
 869 obtained consistently from the continuity equation.

870

871 There are two ways of solving the BP+ system (67), as follows

872 (1) BP+, Newton/Picard iteration version:

873 If $w = \hat{w}(x_i)$ is some arbitrary specified function of position, then (65) becomes a
 874 nonlinear set of n_u equations that may be solved for the horizontal velocity u using
 875 Newton iteration, as follows

$$876 \quad \hat{M}_{UU}(u^K, \hat{w})\Delta u + \hat{R}_U(u^K, \hat{w}) = 0, \quad (68)$$

877 where $\hat{M}_{UU}(u, \hat{w}) = \partial \mathcal{M}_U(u, \hat{w}) / \partial u$, $\Delta u = u^{K+1} - u^K$, and K is the iteration index. In

878 particular, if we choose $\hat{w} = w^K$, where w^K is the horizontal velocity from the previous

879 iteration (i.e., $w^K = w(u^K)$ from (58), where u^K is the horizontal velocity from the

880 previous iteration), we obtain the following Picard iteration:

Starting from $\kappa = 0$, choose an initial guess, $u^0 \neq 0$,

$$\text{Do: } w^K = w(u^K) = M_{pw}^{-1} M_{pu} u^K,$$

$$881 \quad \text{Solve } \hat{M}_{UU}(u^K, w^K)\Delta u + \hat{R}_U(u^K, w^K) = 0, \quad (69)$$

$$u^{K+1} = u^K + \Delta u,$$

$$\kappa = \kappa + 1,$$

Repeat until convergence.

882 The advantage of this method is that iteration is rapid since each iteration step is
 883 equivalent to the short Newton step of the standard Blatter-Pattyn model, (36). On the
 884 other hand, as a Picard iteration, its convergence is expected to be only linear.

885

886 (2) BP+, Quasi-variational, Newton iteration version:

887 Although a variational principle does not exist, it is still possible to make use of
 888 Newton-Raphson iteration to obtain second order convergence. To do this, we treat (67)
 889 as a single multidimensional nonlinear system and solve it using Newton-Raphson
 890 iteration, as follows

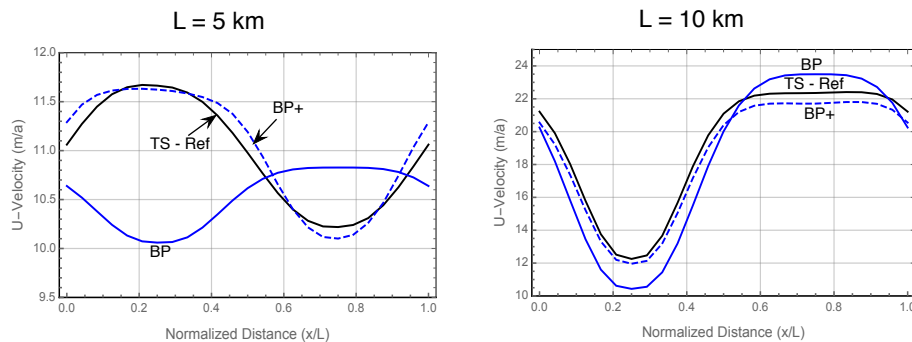


891
$$\begin{bmatrix} \hat{M}_{UU}(u^K, w^K) & \hat{M}_{UW}(u^K, w^K) \\ M_{PU} & M_{PW} \end{bmatrix} \begin{bmatrix} \Delta u \\ \Delta w \end{bmatrix} + \begin{bmatrix} \hat{R}_U(u^K, w^K) \\ \hat{R}_P(u^K, w^K) \end{bmatrix} = 0, \quad (70)$$

892 where $\hat{M}_{UU}(u, w) = \partial \hat{R}_U(u, w) / \partial u$ and $\hat{M}_{UW}(u, w) = \partial \hat{R}_U(u, w) / \partial w$. The convergence is
 893 quadratic once in the basin of attraction but each iteration is more expensive than in the
 894 Picard version because the linear system (70) is approximately double the size of the one
 895 in (69). It remains to be seen which version proves to be preferable in practice.

896

897 Both BP+ versions converge to the same solution. Fig. 9 compares the upper
 898 surface u-velocity from the improved Blatter-Pattyn (BP+) approximation to the standard
 899 Blatter-Pattyn approximation and to a reference exact Stokes calculation. The RMS u-
 900 Error of the BP+ approximation relative to the exact Stokes case is shown in Fig. 12. The
 901 BP+ approximation is noticeably more accurate than the BP approximation, especially so
 902 in the $L = 5$ km case where the Blatter-Pattyn solution bears no resemblance to the
 903 correct solution while the BP+ approximation retains very good accuracy. This is
 904 confirmed by the RMS u-Error results in Fig. 12.



905

906 **Figure 9.** Comparing Approximations. Test B, Upper surface u-velocity.

907 TS-Ref: Transformed Stokes; BP: Blatter-Pattyn; BP+: Improved Blatter-Pattyn.

908

Resolution: 24x24.

909

910 The two versions depend either on solving the continuity equation to obtain

911 $w = w(u)$, or the use of a grid that incorporates such a solvable continuity equation.

912 Solution of the continuity equation to obtain w may already be available for the purpose
 913 of temperature advection in production code packages that either incorporate or are based
 914 on the Blatter-Pattyn approximation. Thus, these new approximations, and particularly
 915 the Newton/Picard version, may be especially attractive for use in such codes since they

916 substantially improve the accuracy of the basic Blatter-Pattyn model, as seen in Fig. 9, at
917 little or no additional cost.

918

919 **6.2.2 A “Dual-Grid” Transformed Stokes Approximation**

920

921 In §6.2.1, the BP+ approximation was based on directly approximating or lagging the
922 vertical velocity w in the second invariant $\tilde{\epsilon}^2$ in the transformed functional $\tilde{\mathcal{A}}$. Here we
923 take a different approach and instead approximate the continuity equation in the
924 transformed Stokes model, which indirectly approximates w . To do this we discretize
925 the continuity equation on a grid that is coarser than the one used for the momentum
926 equations and then interpolate the vertical velocity to the appropriate locations on the
927 finer grid. This reduces the number of unknown variables in the problem, making it
928 cheaper to solve but hopefully without much loss of accuracy. As described in Appendix
929 B, our test problem grids are logically rectangular, divided into n cells horizontally and
930 m cells vertically, thus allowing considerable freedom to specify the coarse grid. The
931 coarse grid is constructed by dividing the fine grid into s equal segments in each
932 direction. This presupposes that the integers n and m are each divisible by s , such that
933 there are s^2 coarse cells in total, with each coarse cell containing nm/s^2 fine cells. The
934 primary grid (i.e., the fine grid) was chosen to have $n = m = 24$, resulting in a reference
935 24×24 fine grid, so as to maximize the number of different coarse grids that may be
936 used for this test. Coarse grids were constructed using $s = 2, 3, 4, 6$, and this resulted in
937 fine/coarse grid combinations labeled by $24 \times 12, 24 \times 8, 24 \times 6, 24 \times 4$, respectively.

938 Similar to a P1-E0 fine grid, coarse grid vertical velocities w are located at vertices and
939 pressures at vertical edges. Fig. 10 illustrates the case of a single coarse and four fine
940 quadrilateral cells for a grid fragment with $n = m = 2$ and $s = 1$. For the Test B problem,
941 using direct substitution for basal boundary conditions, there will be nm u-variables and

942 nm/s^2 w- and p-variables each, for a total of $nm(1 + 2/s^2)$ unknown variables,

943 considerably fewer than the $3nm$ variables in the full resolution (i.e., fine grid) case,
944 depending on the value of s . The coarse grid terms in the functional that are affected,

945 $\tilde{P}(\partial u/\partial x + \partial w/\partial z)$ and $\partial w/\partial x$, are computed using coarse grid variables and

946 interpolated to the fine grid. We will consider two versions of the approximation

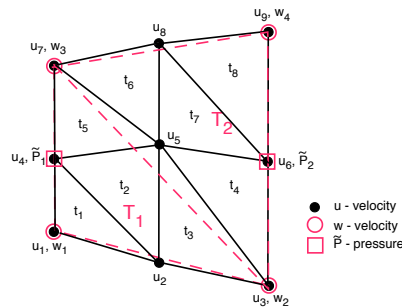
947 depending on how the coarse grid terms are calculated and distributed on the fine grid.

948



949 (1) Approximation A, Bilinear interpolation:

950 Referring to Fig. 10, the four velocities at the vertices of the coarse grid
 951 quadrilateral, i.e., u_1, u_3, u_7, u_9 and w_1, w_2, w_3, w_4 , are used to obtain u, w at the remaining
 952 five vertices of the fine grid by means of bilinear interpolation. Thus, the five velocities
 953 u_2, u_4, u_5, u_6, u_8 are obtained in terms of vertex velocities u_1, u_3, u_7, u_9 , and similarly for the
 954 w velocities. The resulting complete set of fine grid variables, interpolated from coarse
 955 grid variables, are used calculate the divergence $D = (\partial u / \partial x + \partial w / \partial z)$ and the quantity
 956 $\partial w / \partial x$ in each of the eight triangular elements t_1, t_2, \dots, t_8 of the fine grid. Coarse grid
 957 pressures \tilde{P}_1, \tilde{P}_2 are associated with the coarse grid triangles T_1, T_2 . The products $\tilde{P}_1 D$ in
 958 elements t_1, t_2, t_3, t_5 and $\tilde{P}_2 D$ in elements t_4, t_6, t_7, t_8 are then accumulated over the entire
 959 grid to obtain $\tilde{P}(\partial u / \partial x + \partial w / \partial z)$ for use in the transformed functional $\tilde{\mathcal{A}}$. Similarly, the
 960 quantity $\partial w / \partial x$ is computed in the fine grid elements from coarse grid variables for use
 961 in the second invariant $\tilde{\mathcal{E}}^2$.



962

963

964 **Figure 10.** A Sample of a Coarse/Fine P1-E0 Grid for the Dual-Grid Approximation.

965 Resolution: $n = m = 2, s = 1$. Coarse grid is in red, fine grid in black.

966

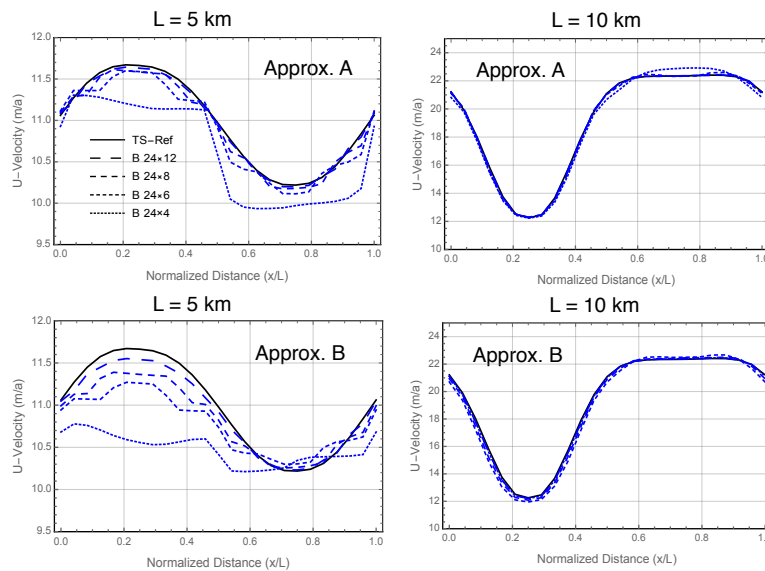
967 (2) Approximation B, Linear interpolation:

968 In this version, the three velocities at the vertices of the two coarse grid triangles
 969 T_1 and T_2 , i.e., u_1, u_3, u_7 and w_1, w_2, w_3 in T_1 , and u_7, u_3, u_9 and w_3, w_2, w_4 in T_2 ,
 970 approximate the divergence $D = (\partial u / \partial x + \partial w / \partial z)$ and the quantity $\partial w / \partial x$ as constant
 971 values in the two coarse triangles. The constant quantities $\tilde{P}_1 D, \tilde{P}_2 D$ are then
 972 accumulated over the entire grid. The constant quantity $\partial w / \partial x$ in each coarse triangle is



973 then distributed to each of the eight fine grid elements t_1, t_2, \dots, t_8 depending on whether
974 the centroid of the fine triangular element is in T_1 or T_2 . As in the previous case, this is
975 then used in the second invariant $\tilde{\epsilon}^2$ when evaluating the transformed functional $\tilde{\mathcal{A}}$.
976

977 While the number and type of unknown variables is the same in the two versions,
978 they differ considerably in accuracy, as is seen in Figs. 11 and 12. Fig. 11 compares the
979 upper surface u-velocity in both version, Approximations A and B, for the four coarse
980 grid combinations and the reference 24x24 fine grid calculation. Fig. 12 compares the
981 overall accuracy the same way by means of the RMS u-Error. As might be expected, the
982 accuracy of Approx. A is better than the accuracy of Approx. B, particularly in the case
983 when $L = 10$ km. Both versions are more accurate than the Blatter-Pattyn and BP+
984 approximations, except at the lowest 24x4 resolution when only the Approx. A version
985 retains that distinction.

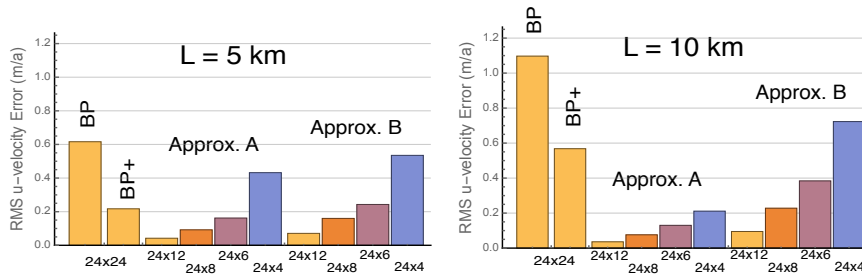


986 **Figure 11.** Comparing Approximations A and B. Test B. Upper surface u-velocity.
987 TS-Ref: Reference Stokes 24x24; Fine/Coarse resolutions (r x R): 24xR, R=12, 8, 6, 4.
988
989

990 In summary, the dual-grid approximation improves on the Blatter-Pattyn
991 approximation in both versions and at all resolutions, as seen in Fig. 12. Compared to the
992 BP+ approximations, here the vertical momentum equation is retained, although in
993 approximated form. In fact, the solution procedure here is very similar to that of the
994 unapproximated Stokes model except that the dimensions of the pressure and the vertical



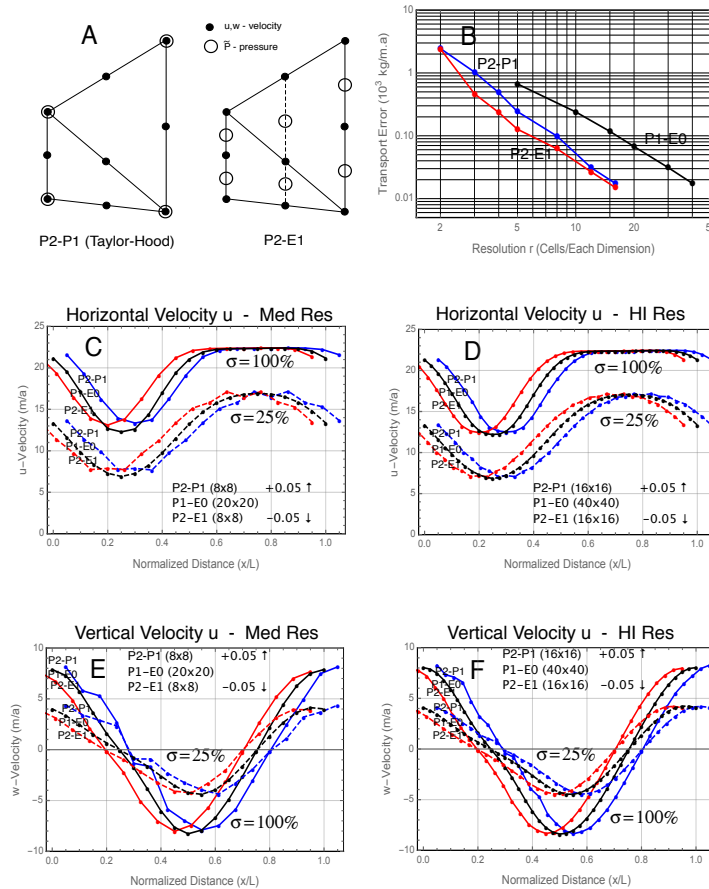
995 velocity variables are reduced. Despite the differences with the unapproximated case, the
 996 arguments in Appendix D regarding stability extend to the case $n_u > n_w = n_p$ appropriate
 997 for the dual-grid approximation. As argued in Appendix D, provided the solvability
 998 condition $n_w = n_p$ holds on the coarse grid, the “reduced” continuity equation may be
 999 solved for the coarse vertical velocity in terms of the fine horizontal velocity
 1000 variables, $w = w(u)$, and in turn, the coarse pressure may be obtained in terms of the fine
 1001 horizontal velocity variables, $p = p(u)$, as in (79). As a result, pressure may be
 1002 eliminated in the dual grid version of the functional, converting the variational
 1003 formulation into a stable minimization problem. Thus, the solvability condition still
 1004 applies, but this time it applies to the coarse grid.



1005
 1006 **Figure 12.** Comparing RMS u-Error in Different Approximations, Test B,
 1007 Resolutions (r x R): Approx. BP, BP+: 24x24; Approx. A, B: 24xR, R=12, 8, 6, 4.
 1008

1009 **7. Second-Order Discretizations**

1010
 1011 So far we have been using first-order elements, primarily P1-E0. However, in current
 1012 practice Stokes models are often based on the popular second-order Taylor-Hood P2-P1
 1013 element (Leng et al., 2012; Gagliardini et al., 2013). The two-dimensional P2-P1
 1014 element, illustrated in Fig. 13A, has velocities on element vertices and edge midpoints
 1015 and pressures on element vertices, resulting in a quadratic velocity and linear pressure
 1016 within the element. The element satisfies the conventional inf-sup stability condition
 1017 (Elman et al., 2014) but not the solvability condition (56). For example, in Test B with
 1018 direct substitution for basal boundary conditions, the number of vertical velocity
 1019 variables in the Taylor-Hood element, $n_w = 4nm$, is typically much larger than the
 1020 number of pressure variables, $n_p = n(m+1)$, where n, m have been defined previously.



1021
 1022 **Figure 13.** Comparing second-order discretizations based on the P2-P1 and P2-E1
 1023 elements from panel A to first-order discretizations using the P1-E0 element running Test
 1024 B with $L=10$ km. For simplicity, only transformed Stokes calculations are compared;
 1025 standard Stokes results behave similarly. Panel B compares the relative accuracy of the
 1026 various schemes with increasing resolution, while panels C through F compare the
 1027 horizontal and vertical velocities at medium and maximum resolutions, i.e., $r = 8, 16$ for
 1028 second-order and $r = 20, 40$ for first-order cases. Plots labeled $\sigma = 100\%$ indicate the
 1029 upper surface while dashed plots labeled $\sigma = 25\%$ indicate surfaces a quarter of the way
 1030 up from the bottom.

1031
 1032 Stokes models work well with a Taylor-Hood grid, as illustrated in Fig. 13, where
 1033 both P2-P1 and P1-E0 models converge to a common Test B solution, but models that
 1034 require the solvability condition (56) will not work on a P2-P1 grid, as discussed in
 1035 connection with the extended Blatter-Pattyn approximation in §4.3.3. For these



1036 applications an alternative will be needed if one wishes to use a second order
1037 discretization. An alternative second-order element, consistent with an invertible
1038 continuity equation, can be created by modifying the Taylor-Hood element to produce the
1039 P2-E1 element illustrated in Fig. 13A. This element is second-order for velocities and
1040 linear for pressure, just like the P2-P1 element, but the pressure is edge-based, as in the
1041 P1-E0 element. The pressure is located midway between the velocities on the vertical
1042 cell edges, including an “imaginary” vertical edge joining the velocities in the middle of
1043 the vertical column as shown in Fig. 13A. Since pressures are collinear with vertical
1044 velocities along vertical grid edges as in the P1-E0 element, the analysis in Appendix C,
1045 §C2, demonstrates that element P2-E1 also satisfies the solvability condition (56).
1046 Preferably, as explained in Appendix C, §C3, a P2-E1 grid is constructed using vertical
1047 columns of quadrilaterals. A three-dimensional analog of this element exists and is
1048 presented in Appendix C.

1049

1050 **Remark #2:** In addition to the P2-E1 element, it is possible to construct other elements
1051 that feature an invertible continuity equation with second-order accurate velocities. Thus,
1052 noting that there are $2nm$ triangular elements in a Test B problem grid, it is sufficient
1053 that each triangular element contains two pressures, resulting in the same total number of
1054 vertical velocity and pressure variables, namely, $n_w = n_p = 4nm$. The pressure will not be
1055 linear within the element but this is unimportant since, as noted before, pressure has no
1056 physical significance.

1057

1058 Fig. 13B shows the approximate error of the ice transport T from (60) as a
1059 function of grid refinement for the second-order P2-P1 and P2-E1 grids in transformed
1060 Stokes Test B calculations, together with similar results for the first-order P1-E0 grid
1061 from Fig. 3, for comparison. Calculation of the error $E = \|T - T_R\|$, as defined in §5.1, is
1062 difficult because we do not have the converged value of the transport T_R . To estimate it,
1063 we use Richardson extrapolation, assuming a rate of convergence proportional to r^{-c} ,
1064 where r is the resolution and c is the order of convergence, taken to be either $c = 2$ in a
1065 first order model and $c = 3$ in a second order model. This gives a reasonable estimate of
1066 the magnitude of the error as plotted in Fig. 13B. We note that both second order models
1067 show approximately the same error at resolution $r = 16$ as the first order P1-E0 model at
1068 resolution $r = 40$, and similarly for coarser resolutions such as $r = 8$ and $r = 20$,
1069 respectively. However, although here the computational costs are not representative, it is

1070 safe to say that these second-order calculations are considerably more expensive than the
1071 first-order calculations at comparable resolution or accuracy.

1072

1073 Panels C, D in Fig. 13 compare the u-velocities, and panels E, F compare the w-
1074 velocities, respectively, from several Test B calculations using the two second-order
1075 models in comparison with first-order P1-E0 model results from Fig. 3. Each panel
1076 shows results from the upper surface ($\sigma = 100\%$) in solid lines and results from a surface
1077 a quarter of the way up from the bottom ($\sigma = 25\%$) in dashed lines. Panels C, E show
1078 results from medium resolution calculations ($r = 8, 20$ in the second-order and first-order
1079 calculations, respectively) and panels D, F show the corresponding results from the
1080 higher resolution calculations ($r = 16, 40$). At these resolutions the accuracy of the first-
1081 and second-order calculations is very similar so for clarity the second-order results are
1082 displaced horizontally from the first-order results by 0.05 nondimensional units. The P2-
1083 E1 results in magenta are displaced to the left and the P2-P1 results in blue are displaced
1084 to the right. In general, models satisfying the solvability condition, namely the P1-E0
1085 and P2-E1 models, are better behaved than the Taylor-Hood model, particularly in the
1086 vertical velocity results, panels E and F, where velocity oscillations are present in the P2-
1087 P1 results. This is presumably related to the well-known “weak” mass conservation of
1088 the Taylor-Hood element. This problem is greatly improved by “enriching” the pressure
1089 space with constant pressures in each triangular element (Boffi et al., 2012). In the 2D
1090 Test B problem this increases the number of pressure variables from $n_p = n(m+1)$ in the
1091 basic Taylor-Hood element to $n(3m+1)$, much closer to the $4nm$ needed to satisfy the
1092 solvability condition. On the other hand, it should be noted that the pressure in the P2-E1
1093 case is highly oscillatory while in the P2-P1 case it is well behaved. However, this is not
1094 at all concerning since, as mentioned earlier in Remark #2, the transformed pressure, a
1095 Lagrange multiplier, has no physical significance.

1096

1097 **8. Summary**

1098

1099 This paper introduces two main innovations. Together, the two innovations expand the
1100 scope of traditional methods used in ice sheet modeling. The first innovation is a
1101 transformation of the ice sheet Stokes equations into a form that closely resembles the
1102 Blatter-Pattyn approximate model. This creates the ability to easily convert from one
1103 model to the other. The variational formulation of the Blatter-Pattyn approximation

1104 differs from the corresponding formulation of the transformed Stokes model only by the
1105 absence of the vertical velocity w in the second invariant of the strain rate tensor. This
1106 makes it possible to create new Stokes approximations by focusing on the smallness of
1107 vertical velocity compared to other terms in the variational functional. Two such
1108 approximations are presented, the BP+ approximation and the dual-grid approximation,
1109 which are cheaper than full-Stokes and more accurate than Blatter-Pattyn. Both
1110 approximations are based on using an approximate vertical velocity that is obtained
1111 inexpensively for this purpose, in general by solving the continuity equation for the
1112 vertical velocity in terms of the horizontal velocity components. In the variational
1113 formulation, the continuity equation is obtained by variation with respect to the pressure,
1114 yielding a system of n_p equations to solve for the n_w vertical velocity variables. Thus,
1115 vertical velocity can only be obtained from the solution of the discrete continuity
1116 equation if the number of unknown vertical velocity variables is equal to the number of
1117 unknown pressure variables, i.e., $n_w = n_p$. This is called the solvability condition.

1118

1119 The second innovation is the introduction of finite element grids in which the
1120 solvability condition is satisfied. These grids incorporate a decoupled and invertible
1121 discrete continuity equation. This has two important consequences. The first is that it
1122 allows for the numerical solution of the continuity equation for the vertical velocity in
1123 terms of the horizontal velocity components, $w = w(u, v)$, which is a prerequisite in the
1124 different approximations made possible by the transformed Stokes formulation. A
1125 second very important consequence is that invertibility of the continuity equation and the
1126 availability of the vertical velocity in terms of the horizontal velocity components can be
1127 used to remove the need for pressure as a Lagrange multiplier. Removing the pressure
1128 from the system of Stokes equations, or from the variational functional, means that a
1129 Stokes problem discretized with such a grid becomes a well-behaved minimization
1130 problem rather than a mixed or saddle-point problem. This eliminates the need for the
1131 inf-sup or LBB condition that is normally required to be satisfied in finite element
1132 formulations. Some examples of such grids for use in both 2D and 3D are given in
1133 Appendix C. An important case is the P1-E0 grid that has been used in most of the test
1134 problems in this paper. To construct such grids we can focus on the term involving
1135 pressure in the variational functionals (15) and (33) in isolation from the other terms, as is
1136 done in (64). The pressure may then be considered a finite element “test function”,
1137 allowing us to construct appropriate test functions that yield n_w independent equations



1138 corresponding to the linear system of continuity equations (57), which is sufficient to
1139 solve for the vertical velocity in terms of the horizontal velocity components. This is
1140 already done in MALI (Hoffman et al., 2018), an ice sheet model based on the Blatter-
1141 Pattyn approximation, to obtain the vertical velocity w needed for the advection of ice
1142 temperature (Mauro Perego, private communication).

1143

1144 We have also introduced some minor innovations in the implementation of the
1145 frictional tangential sliding boundary condition that is often challenging to implement
1146 numerically. Implementation directly into the Stokes equations involves the formation of
1147 the normal component of the stress force at the boundary. This is extremely complex
1148 (e.g., see DPL, 2010). Appendix A describes an alternative that avoids this complication.
1149 The variational formulation makes it possible to also implement this boundary condition
1150 using Lagrange multipliers, but this may not be desirable because it introduces extra
1151 variables. A much more attractive alternative is the use of the no-penetration condition in
1152 the form given by (14) to eliminate the vertical velocity by direct substitution along the
1153 frictional portion of the basal boundary, as discussed in connection with the functional
1154 (15). This automatically enforces both the frictional sliding condition and the no-
1155 penetration condition.

1156

1157 Finally, we need to point out that no cost comparisons have been presented. This
1158 is because the present calculations were made on a personal computer using the program
1159 Mathematica, which is not at all representative of the computer hardware or the methods
1160 that are used in practical ice sheet modeling. Furthermore, no effort was made to
1161 optimize the calculations or to take advantage of parallelization. As a result, cost
1162 comparisons would have been highly misleading.

1163

1164 **Code Availability**

1165

1166 All calculations were made using the Wolfram Research, Inc. program Mathematica in a
1167 development environment. No production code is available.

1168

1169 **Competing Interests**

1170

1171 The author has acknowledged that there are no competing interests.

1172



1173 **Acknowledgements**

1174

1175 I am grateful to Steve Price, and especially to Mauro Perego and William (Bill)
1176 Lipscomb for many helpful comments and suggestions that helped to improve the paper.

1177

1178 **References**

1179

1180 Auricchio, F., da Veiga, L.B., Brezzi, F., and Lovadina, C.: Mixed Finite Element
1181 Methods, In Encyclopedia of Computational Mechanics Second Edition (Eds E. Stein, R.
1182 de Borst, and T.J.R. Hughes), John Wiley & Sons, Ltd., 2017.

1183

1184 Blatter, H.: Velocity and Stress Fields in Grounded Glaciers: A Simple Algorithm for
1185 Including Deviatoric Stress Gradients, *J. Glaciol.*, 41, 333-344, 1995.

1186

1187 Boffi, D., Cavallini, N., Gardini, F., and Gastaldi, L.: Local Mass Conservation of Stokes
1188 Finite Elements, *J. Sci. Comput.*, 52, 383–400, 2012.

1189

1190 Cheng, G., Lötstedt, P., and von Sydow, L.: A Full Stokes Subgrid Scheme in Two
1191 Dimensions for Simulation of Grounding Line Migration in Ice Sheets Using Elmer/ICE
1192 (v8.3), *Geosci. Model Dev.*, 13, 2245-2258, 2020.

1193

1194 Dukowicz, J.K., Price, S.F., and Lipscomb, W.H.: Consistent Approximations and
1195 Boundary Condition for Ice Sheet Dynamics from a Principle of Least Action, *J. Glaciol.*,
1196 56, 480-496, 2010.

1197

1198 Dukowicz, J.K., Price, S.F., and Lipscomb, W.H.: Incorporating Arbitrary Basal
1199 Topography in the Variational Formulation of Ice Sheet Models, *J. Glaciol.*, 57, 461-467,
1200 2011.

1201

1202 Dukowicz, J.K.: Reformulating the Full-Stokes Ice Sheet Model for a More Efficient
1203 Computational Solution, *The Cryosphere*, 6, 21-34, 2012.

1204

1205 Elman, H.C., D.J. Silvester, and A.J. Wathen, 2014: *Finite Elements and Fast Iterative*
1206 *Solvers: With Applications in Incompressible Fluid Dynamics*, 2nd Ed., Oxford
1207 University Press, 494 pp.



1208

1209 Gagliardini, O., and Zwinger, T.: The ISMIP-HOM Benchmark Experiments Performed
1210 Using the Finite-Element Code Elmer, *The Cryosphere*, 2, 67–76, 2008.

1211

1212 Gagliardini, O., Zwinger, T., Gillet-Chaulet, F., Durand, G., Favier, L., de Fleurian, B.,
1213 Greve, R., Malinen, M., Martín, C., Råback, P., Ruokolainen, J., Sacchettini, M., Schäfer,
1214 M., Seddik, H., and Thies, J.: Capabilities and Performance of Elmer/Ice, a New-
1215 Generation Ice Sheet Model, *Geosci. Model Dev.*, 6, 1299–1318, doi:10.5194/gmd-6-
1216 1299-2013, 2013.

1217

1218 Greve, R. and Blatter, H.: *Dynamics of Ice Sheets and Glaciers*, Springer-Verlag, Berlin
1219 Heidelberg, 2009.

1220

1221 Heinlein, A., Perego, M., and Rajamanickam, S.: FROSch Preconditioners for Land Ice
1222 Simulations of Greenland and Antarctica, *SIAM J. Sci. Comput.*, 44, V339-B367, doi:
1223 10.1137/21M1395260, 2022.

1224

1225 Hoffman, M. J., Perego, M., Price, S. F., Lipscomb, W. H., Zhang, T., Jacobsen, D.,
1226 Tezaur, I., Salinger, A. G., Tuminaro, R., and Bertagna, L.: MPAS-Albany Land Ice
1227 (MALI): A Variable-Resolution Ice Sheet Model for Earth System Modeling Using
1228 Voronoi Grids, *Geosci. Model Dev.*, 11, 3747–3780, doi:10.5194/gmd-11-3747-2018,
1229 2018.

1230

1231 Hood, P. and Taylor, C.: Numerical Solution of the Navier-Stokes Equations Using the
1232 Finite Element Technique, *Comput. Fluids*, 1, 1-28, 1973.

1233

1234 Larour, E., Seroussi, H., Morlighem, M., and Rignot, E.: Continental scale, high order,
1235 high spatial resolution, ice sheet modeling using the Ice Sheet System Model (ISSM), *J.*
1236 *Geophys. Res.*, 117, 1–20, doi:10.1029/2011JF002140, 2012.

1237

1238 Leng, W., Ju, L., Gunzburger, M., Price, S., and Ringler, T.: A Parallel High-Order
1239 Accurate Finite Element Nonlinear Stokes Ice Sheet Model and Benchmark Experiments,
1240 *J. Geophys. Res.*, 117, 2156–2202, doi:10.1029/2011JF001962, 2012.



1241

1242 Lipscomb, W.H., Price, S.F., Hoffman, M.J., Leguy, G.R., Bennett, A.R., Bradley, S.L.,
1243 Evans, K.J., Fyke, J.G., Kennedy, J.H., Perego, M., Ranken, D.M., Sacks, W.J., Salinger,
1244 A.G., Vargo, L.J., and Worley, P.H.: Description and Evaluation of the Community Ice
1245 Sheet Model (CISM) v. 2.1, *Geosci. Model Dev.*, 12, 387-424, 2019.

1246

1247 Nowicki, S.M.J. and Wingham, D.J.: Conditions for a Steady Ice Sheet-Ice Shelf
1248 Junction, *Earth Planet. Sci. Lett.*, **265**(1-2), 246-255, 2008.

1249

1250 Pattyn, F.: A New Three-Dimensional Higher-Order Thermomechanical Ice Sheet
1251 Model: Basic Sensitivity, Ice Stream Development, and Ice Flow across Subglacial
1252 Lakes, *J. Geophys. Res.*, 108(B8), 2382, 2003.

1253

1254 Pattyn, F., Perichon, L., Aschwanden, A., Breuer, B., de Smedt, B., Gagliardini, O.,
1255 Gudmundsson, G.H., Hindmarsh, R.C.A., Hubbard, A., Johnson, J.V., Kleiner, T.,
1256 Konovalov, Y., Martin, C., Payne, A.J., Pollard, D., Price, S., Ruckamp, M., Saito, F.,
1257 Soucek, O., Sugiyama, S., and Zwinger, T.: Benchmark Experiments for Higher-Order
1258 and Full-Stokes Ice Sheet Models (ISMIP-HOM), *The Cryosphere*, 2, 95-108, 2008.

1259

1260 Perego, M., Gunzburger, M., and Burkardt, J.: Parallel Finite-Element Implementation
1261 for Higher-Order Ice-Sheet Models, *J. Glaciol.*, 58, 76-88, 2012.

1262

1263 Rückamp, M., Kleiner, T., and Humbert, A.: Comparison of ice dynamics using full-
1264 Stokes and Blatter-Pattyn approximation: application to the Northeast Greenland Ice
1265 Stream, *The Cryosphere*, 16, 1675-1696, 2022.

1266

1267 Schoof, C.: Coulomb friction and other sliding laws in a higher order glacier flow model,
1268 *Math. Models. Meth. Appl. Sci.*, 20(1), 157-189, 2010.

1269

1270 Schoof, C. and Hewitt, I.: Ice-Sheet Dynamics, *Annu. Rev. Fluid Mech.*, 45, 217-239,
1271 2013.

1272



1273 Schoof, C. and Hindmarsh, R.C.A.: Thin-Film Flows with Wall Slip: An Asymptotic
1274 Analysis of Higher Order Glacier Flow Models, *Quart. J. Mech. Appl. Math.*, 63, 73-114,
1275 2010.

1276

1277 Seroussi, H., Ben Dhia, H., Morlighem, M., Latour, E., Rignot, E., and Aubry, D.:
1278 Coupling Ice Flow Models of Varying Orders of Complexity with the Tiling Method, *J.*
1279 *Glaciol.*, 58, 776-786, 2012.

1280

1281 Tezaur, I. K, Perego, M., Salinger, A. G., Tuminaro, R. S., and Price, S. F.:
1282 Albany/FELIZ: A Parallel, Scalable and Robust, Finite Element, First-Order Stokes
1283 Approximation Ice Sheet Solver Built for Advanced Analysis, *Geosci. Model Dev.*, 8,
1284 1197-1220, 2015.

1285

1286 **Appendix A: The Frictional Sliding Boundary Condition**

1287

1288 The frictional sliding boundary condition requires the specification of the tangential
1289 component of the frictional stress force. Dukowicz et al. (2010) obtain this by defining
1290 the frictional stress force at the basal surface as follows

$$1291 \quad \sigma_{ij} n_j^{(b2)} = (\tau_{ij} - P \delta_{ij}) n_j^{(b2)} = -f_i$$

1292 where σ_{ij} is the stress tensor, δ_{ij} is the Kronecker delta, and f_i is the frictional sliding
1293 force vector from §2.2, and then subtracting out the normal component. The result is

$$1294 \quad (\tau_{ij} - \tau_n \delta_{ij}) n_j^{(b2)} + f_i = 0 \quad (71)$$

1295 where $\tau_n = n_i^{(b2)} \tau_{ij} n_j^{(b2)}$ is the normal component of the stress force. However, the three
1296 components of (71) are not independent because they already satisfy the tangency
1297 condition at the basal surface. Since we already have one component of the basal
1298 frictional boundary condition, namely, the tangency condition (10), we therefore need
1299 only two more conditions and these are typically taken to be the two horizontal
1300 components of (71). This option is problematic because of the need to form the highly
1301 complex quantity τ_n .

1302



1303 A simpler alternative is obtained by simply using the unneeded vertical
1304 component of (71) to eliminate τ_n from the two horizontal components. The vertical
1305 component of (71) gives

$$1306 \quad \tau_n n_z^{(b2)} = \tau_{zj} n_j^{(b2)} + f_z. \quad (72)$$

1307 Substituting this into (71), we obtain the desired two conditions, as follows

$$1308 \quad n_z^{(b2)} \left(\tau_{(i)j} n_j^{(b2)} + f_{(i)} \right) - n_{(i)}^{(b2)} \left(\tau_{zj} n_j^{(b2)} + f_z \right) = 0. \quad (73)$$

1309 This is boundary condition (11) as used in §2.2.

1310

1311 Alternatively, one could use of a Lagrange multiplier Λ in the variational
1312 principle, as is done in (13) and in Dukowicz et al. (2011). This yields the tangency
1313 condition (10) together with

$$1314 \quad \tau_{ij} n_j^{(b2)} + (\Lambda - P) n_i^{(b2)} + f_i = 0. \quad (74)$$

1315 Equation (74) provides three conditions, which, together with (10), is one too many.

1316 However, one of these conditions must be used to determine the quantity $\Lambda - P$.

1317 Contracting (74) with $n_i^{(b2)}$, and using the fact that f_i is tangential to the basal surface,

1318 gives us $\Lambda - P = -\tau_n$, which, when substituted into (74) gives us agreement with (71).

1319 Alternatively, employing the vertical component of (74) to determine $\Lambda - P$, yields

$$1320 \quad \Lambda - P = - \left(f_z + \tau_{zj} n_j^{(b2)} \right) / n_z^{(b2)}. \text{ Substituting this into (74) gives the preferred boundary}$$

1321 condition (73).

1322

1323 **Appendix B: Test Problems**

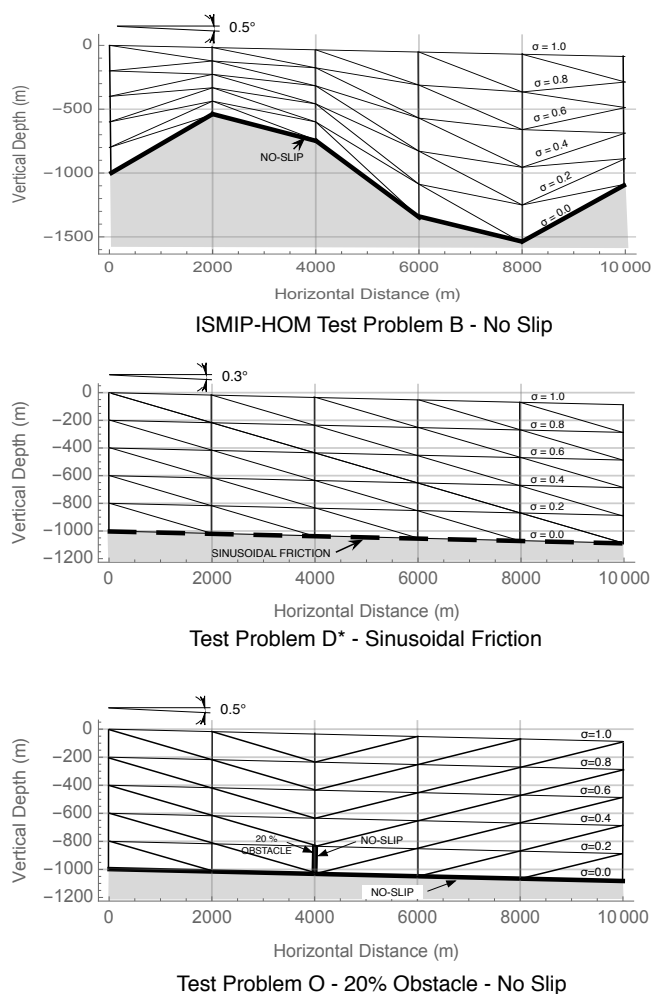
1324

1325 We will use three two-dimensional test problems to demonstrate the new methods. The
1326 geometrical configuration of the three test problem grids is illustrated in Fig. B1. The
1327 first problem, Test B, is actually Exp. B from the ISMIP-HOM benchmark suite (Pattyn
1328 et al., 2008); it features a no-slip condition (infinite friction) on a sinusoidal basal surface.

1329 The second problem, Test D*, featuring sinusoidal friction along a uniformly sloped
1330 plane basal surface, is a replacement with modified parameters for Exp. D from the
1331 benchmark suite. This is because the ice flow in Exp. D is very nearly vertically uniform
1332 (as seen in Fig. 4), which is more characteristic of a shallow-shelf approximation.

1333 Increasing basal friction in Test D* rectifies this. These two test problems, Tests B and

1334 D^* , are used to illustrate and compare the performance of the new transformation versus
 1335 the traditional Stokes formulation.



1336

1337 **Figure B1.** Test problem grids. For clarity, a very coarse 5x5 configuration is used.

1338

1339 A third problem, Test O (for “Obstacle”) has been introduced to illustrate
 1340 adaptive switching between the transformed Stokes and the extended Blatter-Pattyn
 1341 model in a problem where the small aspect ratio assumption underlying the Blatter-Pattyn
 1342 approximation fails locally. Test O has a unique feature, namely, a thin no-slip obstacle,
 1343 located at $x = 4 \text{ km}$ and extending vertically 200 m from the bed (20 % of the ice sheet
 1344 thickness), as illustrated in Fig. B1, which forces the ice flow near the obstacle to adjust
 1345 abruptly. Because of the no-slip boundary conditions along the obstacle surface, a

1346 triangular element in the lee of the obstacle, with one vertical edge and one edge along
1347 the bed, would be a “null” element since all vertex velocities would be zero. This would
1348 create zero stress and therefore a local singularity in ice viscosity in the element. To
1349 avoid this, all elements at the back of the obstacle are “reversed” as compared to the ones
1350 at the front of the obstacle, as shown in Fig. B1.

1351

1352 All tests feature a sloping flat upper surface, given by

1353
$$z_s(x) = -x \tan(\theta), \quad (75)$$

1354 where $\theta = 0.5^\circ$ for Tests B and O, and $\theta = 0.3^\circ$ for Test D* (note that this differs from the
1355 0.1° slope in Test D), with a free-stress upper boundary condition in all cases. The
1356 sinusoidal bottom surface elevation for Test B is specified by

1357
$$z_b(x) = z_s(x) - H_0 + H_1 \sin(\omega x), \quad (76)$$

1358 where the depth $H_0 = 1000 \text{ m}$, $H_1 = 500 \text{ m}$, $\omega = 2\pi/L$, and L is the perturbation
1359 wavelength, which is also the domain length. The bottom surface in Tests D* and O is
1360 parallel to the upper surface so the bottom surface elevation is

1361
$$z_b(x) = z_s(x) - H_0. \quad (77)$$

1362 The length L in the ISMIP-HOM suite ranges from 5 km to 160 km , but here we
1363 consider only the two cases at the high end of the aspect ratio H_0/L range, namely,
1364 $L = 5 \text{ km}$ and $L = 10 \text{ km}$, where the inaccuracy of the Blatter-Pattyn approximation
1365 becomes noticeable. Lateral boundary conditions in all cases are periodic. The spatially
1366 varying friction coefficient for Test D* is given by

1367
$$\beta(x) = \beta_0 + \beta_1 \sin(\omega x), \quad (78)$$

1368 where the friction coefficients are $\beta_0 = \beta_1 = 10^4 \text{ Pa a m}^{-1}$ (these are an order of
1369 magnitude higher than in Test D). Physical parameters used for the test problems are the
1370 same as in ISMIP-HOM, namely, ice-flow parameter $A = 10^{-16} \text{ Pa}^{-3} \text{ a}^{-1}$, ice density
1371 $\rho = 910 \text{ kg m}^{-3}$, and gravitational constant $g = 9.81 \text{ ms}^{-2}$. In general, units are MKS,
1372 except where time is given per annum, which is convertible to per second by the factor
1373 $3.1557 \times 10^7 \text{ s a}^{-1}$.

1374



1375 **Appendix C: Grids Satisfying the Solvability Condition**

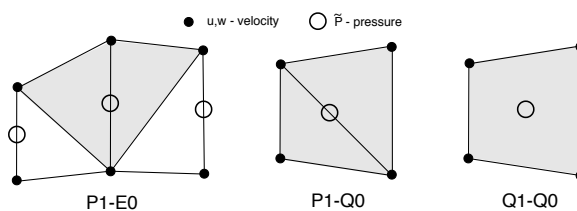
1376 **C1 A Solvable Continuity Equation**

1377

1378 As discussed in §4, the invertibility of the discrete continuity equation, at least in the
 1379 simplest case of direct substitution for basal boundary conditions, requires a special grid
 1380 that satisfies the solvability condition (56), i.e., $n_p = n_w$. Here we discuss several such
 1381 grids and their properties.

1382

1383 The finite element discretization of our test problems, described in Appendix B
 1384 and illustrated in Fig. B1, is constructed using vertical columns of quadrilaterals that are
 1385 subdivided into triangles. Fig. C1 illustrates three different two-dimensional elements on
 1386 triangles or quadrilaterals that may be used to construct grids that may be used to satisfy
 1387 the solvability condition (56) in certain circumstances. The P1-E0 element is quite
 1388 general and satisfies the solvability condition along each vertical grid edge, as will be
 1389 demonstrated in Appendix C, §C2. As noted before, it has velocities located at triangle
 1390 vertices, resulting in a linear velocity distribution within the triangle (P1), and pressure is
 1391 located on the vertical edge of each triangle, resulting in constant pressure over the two
 1392 triangles that share that edge (E0). A second order version of the P1-E0 element, the P2-
 1393 E1 element, is illustrated in Fig. 13A. The two other elements in Fig. C1, i.e., the P1-Q0
 1394 and Q1-Q0 elements, satisfy the solvability condition when used in the grids for our test
 1395 problems, Tests B and D*, but may not do so in other problems. The P1-Q0 element also
 1396 has velocities on triangle vertices for a linear velocity distribution within the triangle
 1397 (P1), but pressure is constant within the two triangles that form a quadrilateral (Q0). The
 1398 element Q1-Q0 has velocities located at quadrilateral vertices and pressure centered in
 1399 the quadrilateral, resulting in a bi-quadratic velocity distribution and a constant pressure
 1400 within the quadrilateral (Q0).



1401

1402 **Figure C1.** Three first-order 2D elements that may be used to satisfy the

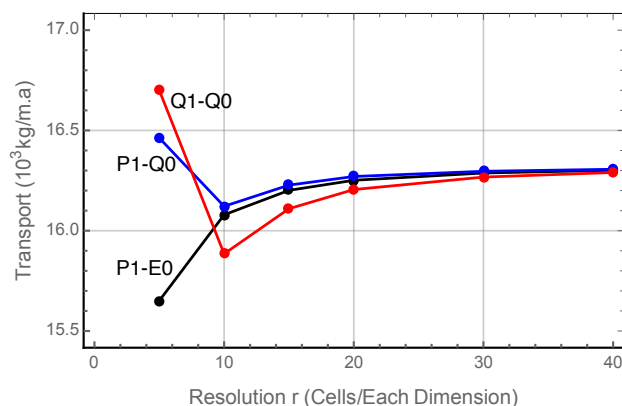
1403

solvability condition, (56), in Tests B and D*.

1404



1405 Fig. C2 shows the convergence of ice transport with grid resolution for Test B
 1406 calculations using these three elements. The solutions are stable and they all converge to
 1407 the same value for the ice transport. The pressure distribution is smooth in the P1-E0
 1408 case, but contains very small fluctuations near the surface in the P1-Q0 and Q1-Q0 cases
 1409 that tend to disappear as the resolution is increased. The Q1-Q0 element is attractive
 1410 because of its simplicity but it has the potential for a pressure null space, resulting in
 1411 pressure checkerboarding (Elman et al., 2014, where the element is called Q1-P0). As a
 1412 result, apparently it is only used in a stabilized form. Here, however, the Q1-Q0 grid
 1413 satisfies the solvability condition in Test B and behaves well. Overall, these results
 1414 confirm our expectation of stability for grids when they satisfy the solvability condition
 1415 as will be discussed in Appendix D. The P1-E0 element is somewhat special because the
 1416 solvability condition (56) is satisfied individually along each vertical edge in grids that
 1417 are composed of this element, as opposed to being satisfied over the entire grid as in the
 1418 other two elements, as we discuss next.



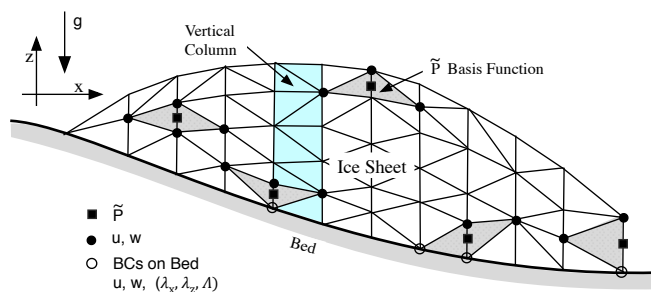
1419
 1420 **Figure C2.** Convergence of Test B ice transport for grids using the three elements
 1421 from Fig. C1. All discretizations are stable and converge to the same solution.

1422
 1423 **C2 Proving that the P1-E0 Element Satisfies the Solvability Condition**

1424 The P1-E0 element from Fig. C1 is used in an example grid in Fig. C3. Note that
 1425 the grid is composed of vertical columns subdivided into triangular elements. To
 1426 demonstrate that the element meets the solvability condition (56) it is sufficient to
 1427 consider a single vertical edge extending from the bottom to the top. Assuming there are
 1428 m edge segments in the vertical direction, there will be $m + 1$ discrete w variables and m
 1429 discrete \tilde{P} variables, such that each \tilde{P} variable is located between a pair of w variables.
 1430 Since the w variable at the bed is specified as a boundary condition, either directly as a
 1431 no-slip condition or in terms of the horizontal velocity component as part of a no-



1432 penetration condition, there will be only m unknown w variables, and therefore $n_w = n_p$
 1433 along each vertical grid edge, and hence over the entire grid, as desired. In case
 1434 Lagrange multipliers are used, there will be $m+1$ unknown discrete w variables (since
 1435 now the basal vertical velocity w is also an unknown). This is matched by m unknown
 1436 \tilde{P} variables, supplemented by one λ_z or one Λ unknown Lagrange multiplier variable,
 1437 depending on the type of boundary condition. Thus, again the number of unknown
 1438 variables equals the number of equations along every vertical edge, thereby satisfying the
 1439 solvability condition whether Lagrange multipliers are used or not. Importantly, this
 1440 means that this element can be used to satisfy the solvability condition irrespective of the
 1441 boundary conditions on quite arbitrary grids, as illustrated in Fig. C3. These arguments
 1442 apply for other versions of the P1-E0 element as well, such as the second order version
 1443 P2-E1 in Fig. 13A or the 3D version in Fig. C4.



1444
 1445

1446 **Figure C3.** An illustration of a 2D edge-based P1-E0 grid, composed of vertical columns
 1447 randomly subdivided into triangles. Pressures are located on the vertical edges.
 1448 The triangulation and the configuration of the associated pressure basis functions
 1449 (shown in gray), is quite general, allowing for a flexible triangulation of the domain.

1450

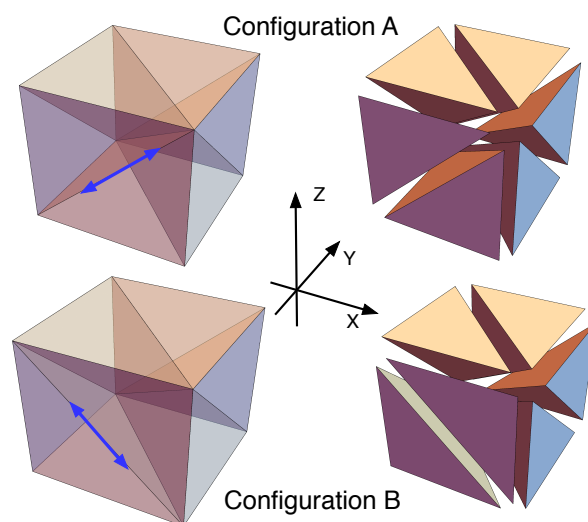
1451 C3 Two- and Three-Dimensional Meshes Based on the P1-E0 Element

1452 The P1-E0 element has been used on the simple test problem grids in Fig. B1 and
 1453 performs well. Moreover, the element has great geometric generality so it may be used
 1454 for quite complicated grids, as in Fig. C3. Generally, there are two triangles associated
 1455 with a pressure variable, one on each side of a vertical edge, except in situations as in Fig.
 1456 C3 where the ice sheet ends at a vertical face. Even in this unusual situation there is no
 1457 problem since the pressure is simply associated with the single triangle on one side of the
 1458 vertical face.

1459



1460 The two-dimensional P1-E0 element has a relatively simple three-dimensional
 1461 counterpart, shown in Fig. C4. The mesh again consists of vertical columns, this time
 1462 composed of hexahedra. Each hexahedron is subdivided into six tetrahedra such that
 1463 each vertical edge is surrounded by from as few as four to as many as eight tetrahedra.
 1464 As in the two-dimensional case, velocity components are collocated at vertices, yielding a
 1465 piecewise-linear velocity distribution in each tetrahedral element, and pressures are
 1466 located in the middle of each vertical edge so that pressure is constant in the tetrahedra
 1467 surrounding that edge. Lagrange multipliers, if used, are located at the vertices on the
 1468 basal surface, yielding a piecewise linear distribution on the basal triangular facet. This
 1469 arrangement also satisfies the solvability condition (56) since pressures and vertical
 1470 velocities are again intermingled along a single line of vertical edges from top to bottom,
 1471 as in the 2D case. Thus, the solvability argument used in the two-dimensional case
 1472 applies, confirming that the 3D version of the P1-P0 element also satisfies the solvability
 1473 condition.



1474
 1475
 1476
 1477
 1478
 1479

Figure C4. Three-dimensional P1-E0 tetrahedral elements that generalize the 2D P1-E0 element of Fig. C1. Configurations A and B differ by having an internal triangular face rotated, as indicated by the blue arrows. Both configurations satisfy the solvability condition.

1480 Fig. C4 shows two of the several possible configurations of a typical hexahedron,
 1481 including an exploded view of each configuration for clarity. The two configurations
 1482 differ in having the internal face of the two forward-facing tetrahedra rotated, creating
 1483 two different forward facing tetrahedra. The remaining six tetrahedra are undisturbed.



1484 Since edges must align when hexahedra (or tetrahedra) are connected, this demonstrates
1485 that the three-dimensional mesh can be flexibly reconnected and rearranged, just as in the
1486 two-dimensional case.

1487

1488 **Remark #3:** A closely related and perhaps simpler three-dimensional P1-E0 element is
1489 one based on the P2-P1 prismatic tetrahedral element used in Leng et al. (2012). A grid
1490 of these elements is composed of vertical columns of triangular prisms, with triangular
1491 faces at the top and bottom, which are then each subdivided into three tetrahedra. As in
1492 Fig. C4, pressures are located on the vertical prism edges.

1493

1494 Meshes composed of P1-E0 elements have another useful property. Since
1495 pressure and vertical velocity variables alternate along vertical grid lines, the matrix-
1496 vector products $M_{wp}P$, $M_{wp}^T w$ in (47), corresponding to $\partial\tilde{P}/\partial z$ and $\partial w/\partial z$ in the
1497 vertical momentum and continuity equations, respectively, consist of simple decoupled
1498 bi-diagonal one-dimensional difference equations along each vertical grid line for
1499 determining pressure, as in (79), and the vertical velocity, as in (58). This should be
1500 particularly advantageous for parallelization.

1501

1502 Just as the two-dimensional second-order P2-E1 element in Fig. 13A is a
1503 generalization of the P1-E0 element, a three-dimensional second-order P2-E1 element
1504 may be constructed as a generalization of the P1-E0 element illustrated in Fig. C4.
1505 Velocities are to be located at the vertices and at midpoints of the tetrahedral edges, and
1506 pressures are to be located halfway between the velocities on vertical edges, including the
1507 imaginary vertical edges through the midpoints of the tetrahedral edges, in the same way
1508 as in the 2D case in Fig. 13A. The P2-E1 element, both 2D and 3D, also satisfies the
1509 solvability condition since the arguments in Appendix C, §C2, apply here also because
1510 pressures are again located midway between vertical velocities along all vertical edges.

1511

1512 **Appendix D: Proving the Stability of a Stokes Problem with an** 1513 **Invertible Continuity Equation**

1514 Here we show that a discretization of a Stokes problem is stable on a grid that
1515 satisfies the solvability condition (56), or equivalently, one that is consistent with an
1516 invertible continuity equation, i.e., (58). This is because such a discretization is
1517 equivalent to the formulation of an unconstrained problem, i.e., a problem without the use
1518 of pressure as a Lagrange multiplier. In fact, such a problem is also equivalent to an



1519 optimization problem, or more specifically, to a minimization problem. To demonstrate
1520 this, consider the full set of discrete Euler-Lagrange equations (47). Recall that the
1521 solvability condition implies the invertibility of M_{wp} , and therefore also the invertibility
1522 of its transpose, M_{wp}^T , i.e., (59). This means that we can solve for the pressure from the
1523 vertical momentum equation, the second equation in (47), to obtain

$$1524 \quad p = -M_{wp}^{-1} \left(M_w(u, w(u)) + F_w \right), \quad (79)$$

1525 where we would use $w(u)$ from (58). Using (79) to eliminate the pressure in the
1526 horizontal momentum equation, we obtain

$$1527 \quad M_U(u, w(u)) - M_{UP} M_{wp}^{-1} \left(M_w(u, w(u)) + F_w \right) + F_U = 0. \quad (80)$$

1528 This is a nonlinear set of equations for just the horizontal velocity u , similar in this
1529 respect to the standard Blatter-Pattyn formulation in that it is no longer a mixed or
1530 saddle-point problem because pressure is absent. As a result, although still a rather
1531 complicated nonlinear problem, it should not suffer from the stability issues discussed in
1532 §4.3.1. Alternatively, using $w = w(u)$ in the functional (46) eliminates the pressure term
1533 because continuity is already satisfied, and one obtains a reduced functional,

$$1534 \quad \mathcal{A}(u) = \mathcal{M}(u, w(u)) + u^T F_U + w(u)^T F_w. \quad (81)$$

1535 This implies that $\mathcal{A}(u)$ is a positive-definite functional involving only the horizontal
1536 velocity components because $\mathcal{M}(u, w(u))$ is positive-definite (see §4.1), which means
1537 that now the Stokes variational formulation represents an optimization, or more
1538 specifically, a minimization problem. It is therefore a well-defined and stable problem
1539 for the horizontal velocities (albeit numerically very expensive). We conclude that the
1540 solution of a Stokes model on a grid satisfying the solvability condition, or equivalently,
1541 one that allows for an invertible discrete continuity equation is stable and well behaved.
1542

1543 Note that the arguments here and in §4 apply to arbitrary values of n_u, n_w, n_p , and
1544 in particular, they apply in the case $n_u > n_w = n_p$ that is relevant to the “dual-grid”
1545 approximation of §6.2.2. As a result, we conclude that the dual-grid approximation is
1546 also stable provided the solvability condition (56) holds on the coarse grid.
1547



1548 **Remark #4:** Instead of the standard formulations of the Stokes problem that include the
1549 pressure, such as (46) or (47), one could consider using the corresponding pressure-free
1550 formulation, (80) or (81), to solve for u , followed by (58) and (79) if one is interested in
1551 the vertical velocity and pressure. This corresponds to a discrete version of the pressure-
1552 free formulation attempted analytically by Dukowicz (2012). However, this formulation
1553 couples together large parts of the grid and produces a dense Hessian matrix when using
1554 Newton-Raphson iteration, thus making the conventional numerical solution extremely
1555 costly and therefore impractical, particularly for large problems.